Near-Global Survey of Effective Droplet Radii in Liquid Water Clouds Using ISCCP Data

QINGYUAN HAN*

Columbia University, New York, New York

WILLIAM B. ROSSOW AND ANDREW A. LACIS

Goddard Institute for Space Studies, New York, New York

(Manuscript received 12 January 1993, in final form 16 August 1993)

ABSTRACT

A global survey of cloud particle size variations can provide crucial constraints on how cloud processes determine cloud liquid water contents and their variation with temperature, and further, may indicate the magnitude of aerosol effects on clouds. A method, based on a complete radiative transfer model for AVHRR-measured radiances, is described for retrieving cloud particle radii in liquid water clouds from satellite data currently available from the International Satellite Cloud Climatology Project. Results of sensitivity tests and validation studies provide error estimates. AVHRR data from *NOAA-9* and *NOAA-10* have been analyzed for January, April, July, and October in 1987 and 1988. The results of this first survey reveal systematic continental and maritime differences and hemispheric contrasts that are indicative of the effects of associated aerosol concentration differences: cloud droplet radii in continental water clouds are about 2–3 μm smaller than in marine clouds, and droplet radii are about 1 μm smaller in marine clouds of the Northern Hemisphere than in the Southern Hemisphere. The height dependencies of cloud droplet radii in continental and marine clouds are also consistent with differences in the vertical profiles of aerosol concentration. Significant seasonal and diurnal variations of effective droplet radii are also observed, particularly at lower latitudes. Variations of the relationship between cloud optical thickness and droplet radii may indicate variations in cloud microphysical regimes.

1. Introduction

Cloud microphysical processes, which control the conversion of water vapor to cloud particles (liquid and ice) and precipitation, provide a key link between the radiative effects of water vapor and clouds and the hydrological cycle, and create several important cloud–climate feedbacks. Study of variations of cloud particle size distribution with other cloud properties and meteorological conditions can be diagnostic of the processes that control cloud radiative properties. Thus, measurements of cloud particle size are usually made during cloud field experiments. Information on cloud microphysical properties is also necessary for better interpretation of satellite remote sensing measurements in terms of the optical properties that affect both the shortwave and longwave radiative fluxes comprising earth's radiation balance. Yet routine measurement of cloud microphysical properties from satellites has not occurred, so that interpretations of satellite observations have been limited and not used to extend the detailed knowledge gained from cloud physics studies to the larger space and time scales relevant to climate.

The different cloud and radiation parameterizations employed in general circulation models (GCMs) cause them to predict widely different cloud radiative effects on the model radiation balance resulting in a large range of cloud-radiative feedbacks on model climates (Cess et al. 1990). One common aspect of these parameterizations is that they are loosely based on the surface and aircraft measurements from several decades of cloud studies, which are still generally limited to daytime in midlatitudes at low altitudes and to land areas or near-coastal marine areas. Cloud properties observed in one region and in one season may differ from those in other regions and in other seasons, however. A recent example of this limitation is the difference between the relationship of cloud water path and temperature inferred from aircraft measurements over midlatitude land areas and that inferred over the whole globe from satellite measurements (Tselioudis et al. 1992). Another example is that some authors report a correlation between cloud optical thickness and cloud particle size (e.g., Curry and Herman 1985), while others find no such dependence (e.g., Stephens 1978). We do not yet know how to generalize our detailed understanding of cloud microphysics.

* Current affiliation: Institute of Atmospheric Sciences, South Dakota School of Mines and Technology, Rapid City, South Dakota.

Corresponding author address: Dr. Qingyuan Han, Institute of Atmospheric Sciences, South Dakota School of Mines and Technology, 501 E. St. Joseph Street, Rapid City, SD 57701-3995.

When considering cloud feedbacks on earth's radiation balance, aerosols introduce additional complications (e.g., Charlson et al. 1992; Hansen and Lacis 1990). Although aerosols can warm the earth under some circumstances (MacCracken et al. 1986), their direct radiative effect is generally a cooling of the surface by reflecting sunlight back to space. Changes in aerosols may also alter cloud microphysical properties and change their effects on the radiation budget. Some observations show aerosols increasing cloud reflectivity by decreasing particle sizes, inhibiting rainfall and prolonging cloud lifetimes (Albrecht 1989), but we do not know how other types of clouds will respond to aerosol changes. The possibility of both microphysical and macrophysical changes in clouds, in general, means that the proper interpretation of the causes of changes in cloud radiative properties requires monitoring many cloud characteristics together.

Satellite measurements of cloud properties began with determinations of cloud amount and, sometimes, cloud-top temperature (pressure or height) and have been extended to inferences of cloud optical thickness (Rossow et al. 1989; Rossow and Lacis 1990). The most extensive measurements of these three cloud properties are being made by the International Satellite Cloud Climatology Project (ISCCP) (Rossow and Schiffer 1991). In the absence of global cloud microphysical information, the ISCCP analysis of visible radiances to infer cloud optical thickness assumes that the effective cloud particle radius of all clouds is 10 μm (Rossow et al. 1991). Such an assumption makes the retrieved values uncertain by 15%–25% for water clouds (Rossow et al. 1989; Nakajima and King 1990) and by 30%–50% for thinner ice clouds because of different ice particle scattering phase functions (Minnis et al. 1993).

Remote sensing of cloud drop size dates to the early 1970s (e.g., Hansen and Pollack 1970; Pollack et al. 1978). Some information on the cloud microstructure can be obtained by observing the spectral variation of the intensity of reflected sunlight in the near infrared (Blau et al. 1966; Hovis and Tobin 1967; Hansen and Pollack 1970). Since then, many case studies of cloud drop size retrievals have been done using different spectral bands (e.g., Twomey and Cocks 1982, 1989; Arking and Childs 1985; Prabhakara et al. 1988; Ackerman and Smith 1990; Wielicki et al. 1990; Nakajima and King 1990; Rawlins and Foot 1990; Nakajima et al. 1991). One problem noted in aircraft investigations is that remote sensing often overestimates droplet sizes in comparison with the in situ measurements (e.g., Rawlins and Foot 1990; Nakajima et al. 1991). This problem is referred to as "abnormal absorption." Recently, Taylor (1992) showed that the atmospheric corrections calculated using LOWTRAN 5, a commonly used radiation code for analysis of remotely sensed radiation, underestimate atmospheric absorption at some wavelengths by as much as ~15% (relative) compared with the newer LOWTRAN 7. He shows that this discrepancy can produce the observed overestimate of the effective cloud particle radius instead of an "abnormal absorption."

Retrieval of cloud particle size in the visible and near IR is accomplished by comparing the relative reflectivity of clouds at two wavelengths with different amounts of cloud droplet absorption (Nakajima and King 1990). The advantage of this ratio approach is that since atmospheric effects are very weak at these wavelengths and surface reflectivity can be specified from clear observations, the relative reflectivity of the clouds depends most on the total amount of cloud material present but not very sensitively on its macroscopic distribution within the instrument field of view. The only visible and near-IR wavelengths at which global measurements from the same instrument are currently available are the AVHRR (Advanced Very High Resolution Radiometer) channels with central wavelengths of 0.6, 0.8, and 3.7 μm. Radiation at 3.7 μm also includes a contribution from thermal emission, which can be determined from the other two AVHRR channels at 10.5 and 11.5 μm.

We have developed a practical scheme to infer cloud particle effective radii (see definition in Appendix) for water clouds (cloud-top temperatures > 273 K) from measurements at 3.7 μm, together with those at 0.6 and 10.5 μm, taken globally by the AVHRR on NOAA polar-orbiting weather satellites. The scheme is applied to AVHRR data already analyzed by ISCCP, described in section 2. The scheme compares the measured radiances to radiative transfer model calculations. The radiative model (section 3a) uses a doubling–adding treatment of multiple scattering in a vertically inhomogeneous medium (Lacis and Hansen 1974) and includes the effects of all major absorbing gases (Lacis and Oinas 1991) to compute synthetic radiances for all AVHRR channels. A method of estimating instrument noise and accounting for its effects has also been developed (Han 1992). The retrieval scheme (section 3b), based on the radiative model, relies on the ISCCP cloud detection and combines the ISCCP-determined cloud optical thickness, cloud-top temperature, surface reflectance, and surface temperature with the 3.7- and 11-μm radiances to retrieve cloud particle size and to revise the cloud optical thickness. In section 4, results from sensitivity tests are used to estimate the magnitude of the most important sources of error. Also, comparisons of retrieved droplet sizes to other measurements of droplet size provide some verification of the method. Section 5 presents the results of a near-global survey obtained from 8 months of data, covering the four seasons, from the AVHRRs on both *NOAA-9* ("afternoon" orbiter) and *NOAA-10* ("morning" orbiter). Comparison of the results from the two polar orbiters provides a preliminary assessment of diurnal variations. These results are summarized and discussed in section 6.

2. Data

a. Data description

The dataset used to retrieve cloud particle sizes is the ISCCP CX data derived from the *NOAA-9* and *NOAA-10* AVHRRs from January, April, July, and October 1987 and 1988. ISCCP CX data are composed of the stage B3 radiance data (Schiffer and Rossow 1985; Rossow et al. 1987), which are *samples* of the original radiances from all five AVHRR channels with viewing and illumination geometry, plus the results of the ISCCP cloud analysis for each original image pixel. We use radiances from channel 1 (0.54–0.80 μm), channel 3 (3.44–4.04 μm), and channel 4 (10.0–11.6 μm). The original image pixels represent an area of about 4×1 km^2 and have been sampled to a spacing of about 30 km. This dataset provides sufficient statistical sampling of the original AVHRR radiances to produce a climatology of cloud properties (e.g., Seze and Rossow 1991) and takes advantage of the ISCCP cloud detection analysis to distinguish cloudy from clear pixels. The ISCCP analysis also provides values of cloud optical thickness, τ, cloud-top temperature, T_C, top pressure, P_C, and surface temperature, T_S. Also included in the CX dataset are earth location, a land–water flag, and a snow/ice flag for each pixel. The atmospheric temperature and humidity profiles used in our retrieval are taken from the ISCCP version of the NOAA TOVS (TIROS Operational Vertical Sounder) data (Rossow et al. 1991).

b. Radiance calibration

ISCCP radiance calibrations for channels 1 and 4 are normalized to that of the *NOAA-7* AVHRR in July 1983; however, the absolute channel 1 calibration was later modified based on comparisons to aircraft measurements over White Sands (Brest and Rossow 1992). The estimated absolute uncertainty of the channel 1 calibration is 5%–10%. The absolute uncertainty of the channel 4 calibration, based on NOAA calibration procedures, is estimated to be 1–2 K near 280–290 K (Brown et al. 1985, 1992); the uncertainty at lower temperatures is larger, based on the observed variability of global statistics, but is still only 2–3 K (Brest and Rossow 1992).

Brown et al. (1985, 1992) have also shown that the uncertainty in the channel 3 calibration at higher temperatures is similar to that for channel 4. We obtained similar estimates by checking the consistency of sea surface temperatures (SST) retrieved from channel 3 and 4 radiances over high-latitude oceans at night, where differences in atmospheric effects are small: at brightness temperatures > 270 K, both channel 3 and 4 SST values agree to within 1 K. Moreover, the channel 3 and 4 SST values from *NOAA-9* and *NOAA-10* in overlapping observations at high latitudes also agree to within 1 K. Noise levels in channel 3 radiances are monitored as part of the analysis procedure (Han 1992); for the datasets used here, the noise level was generally <3%.

c. Validation of the ISCCP analysis

Our analysis builds on the results of the ISCCP cloud detection and radiative analysis of channel 1 and 4 radiances; thus, the accuracy of our results depends on the accuracy of the ISCCP analysis. We summarize ISCCP validation results here.

Since we use individual image pixel results, the accuracy of the ISCCP-determined cloud amount only directly affects our results in one way. Since we infer cloud particle sizes in "cloudy" pixels, our statistics will be affected by any clear pixels that are mistakenly included and only secondarily by cloudy pixels that are excluded. The latter effect is only small if we have included the majority of the clouds in the sample. The detection accuracy of the ISCCP analysis can be assessed by checking the accuracy of clear radiances and by comparison to other measurements of cloud amount. Rossow and Garder (1993b) show the results of several such comparisons and estimate the uncertainty in cloud detections to be about 5%–10% rms. In particular, a detailed comparison of ISCCP and surface observer cloud detections over land areas suggests that <5% of the detections are false, except in winter when the false detections are somewhat more frequent but still <10% (Rossow et al. 1993). Thus, over 90% of the pixels analyzed as clouds are actually clouds and less than 10% of existing clouds have been missed.

A key assumption made in both the ISCCP and our analysis for comparison of radiative transfer model calculations to the measured cloudy radiances is that the instrument field of view (pixel) is covered by a uniform layer of cloud. Thus, the more important "cloud amount" issue concerns how frequently the 4×1 km^2 AVHRR pixels are only partially covered by cloud and how much error in the retrieved droplet radius is caused when subpixel cloud cover variations occur. We discuss this issue in section 4c and test the sensitivity of our results to partial cloud cover.

Validation studies have also provided estimates of the uncertainty in ISCCP surface temperature values that are used in our analysis: about 2 K over oceans and about 4 K over land (Rossow and Garder 1993b). A preliminary study (Rossow et al. 1987) also shows that there is little systematic error in retrieved surface temperatures as a function of satellite zenith angle. Bias errors in the surface temperatures caused by the water vapor dataset and the water vapor absorption coefficient used in the ISCCP analysis are essentially eliminated by the fact that we use the same dataset and absorption coefficient for channel 4 in our analysis to reconstruct the upwelling 10.5-μm radiances.

Uncertainties in ISCCP-retrieved cloud-top temperatures are caused by the treatment of water vapor ef-

fects, cloud effects, and the homogeneity of the cloud properties in a single pixel. The uncertainties associated with water vapor effects will be smaller for cloud-top temperatures than for surface temperatures, since much of the water vapor is below the cloud tops. Neglect of scattering at 10.5 μm produces only small (<3%) errors for *water* clouds, partly because the cloud emission temperature is not very different from the brightness temperature of the upwelling radiation from the surface. Systematic errors of cloud-top temperature as a function of satellite zenith angle are also <3% (Rossow et al. 1987). Both these sources of error are about 2–3 K (Rossow et al. 1989). Errors caused by subpixel cloud variations will be small because of the similarity of brightness temperatures of radiation from clouds and clear sky for low-level clouds, but this source of error is considered further in section 4c.

Since we isolate water clouds using the measured cloud-top temperature, another source of error in our analysis is how much optically thin cirrus cloud contamination can be included in a pixel if we restrict $T_C > 273$ K. We discuss this question in section 4d.

Many sources of uncertainty in retrieval of cloud optical thicknesses are much less than 10% (Rossow et al. 1989). The largest error sources are finite geometry effects for broken clouds, deviations of cloud particle shape from spherical in ice clouds, and deviations of the droplet radii from the 10-μm value assumed in the ISCCP radiative model. We avoid the second error source by focusing on warm, liquid water clouds and explicitly correct the third error during our retrieval of cloud particle radii. Studies of the angular dependence of visible radiances from various cloud types do show some systematic differences with the plane-parallel representation (Coakley and Kobayashi 1989), but overall errors are <10% for the near-nadir viewing geometry used in our analysis (Kobayashi 1993). We also consider this issue in section 4c.

3. Radiation model and retrieval scheme

a. ISCCP retrieval scheme

The radiative transfer model used in our analysis to simulate the AVHRR radiances is described below. It is based on the model developed by Lacis and Hansen (1974) and is the same model used for the ISCCP retrieval scheme (Rossow et al. 1989; Rossow et al. 1991), except for a more precise treatment of the finite bandpass of the AVHRR channels. The ISCCP retrieval has three steps. The TOVS dataset provides atmospheric temperature and humidity profiles for each 2.5° region over the globe every day; these are used with the infrared radiation model to precalculate top-of-atmosphere infrared radiances as a function of cloud-top temperature and satellite viewing zenith angle for opaque (blackbody) clouds. In the first retrieval step, the observed infrared radiance for each cloudy image pixel is compared to the collocated model values to determine the corresponding cloud-top temperature (and pressure) from the TOVS profile. A precalculated database of results from the visible radiation model contains top-of-atmosphere visible radiances as a function of cloud optical thickness, viewing geometry, surface reflectance, and cloud-top pressure. In the second retrieval step, the observed visible radiance for each cloudy image pixel is compared to this database, with cloud-top pressure obtained from the first step and surface reflectance specified from a prior analysis of clear pixel visible radiances. Finally, in the third retrieval step, if the cloud visible optical thickness is <9, the cloud-top temperature is corrected for the effects of partial transmission of infrared radiation from below the cloud, based on the surface temperature specified from a prior analysis of clear pixel radiances. This last step is iterated until the cloud-top temperature/pressure and optical thickness are consistent.

b. Radiation model

Our radiative model atmosphere is divided into 12 vertical, plane-parallel layers that are horizontally homogeneous. For most calculations and illustrations shown in this paper, the temperature, humidity, and ozone abundance profiles used are the global average, tropical, midlatitude summer, and midlatitude winter profiles from the Standard Atmosphere (McClatchey et al. 1972). The temperature and humidity profiles can also be specified from observations. Solar irradiance data are taken from Neckel and Labs (1984) for channel 1 and Thekaekara (1974) for channel 3. The instrument "solar constants" for specific satellite were calculated in the model using the spectral response functions (Rossow et al. 1987) and solar spectra. Molecular scattering is included as Rayleigh scattering. Gaseous absorptions in the model atmosphere are from line absorptions by H_2O, CO_2, O_3, O_2, N_2O, CH_4, and continuum absorptions by H_2O, O_3, N_2. Table 1 indicates which absorbing and scattering components affect each AVHRR channel. The atmosphere is considered to be in local thermal equilibrium and thermal radiation is determined by the emissivity and the Planck function, which varies linearly over each model layer. The correlated k-distribution method (Lacis and Oinas 1991) is used to calculate gaseous absorption in a vertically inhomogeneous, scattering atmosphere. Surface reflectances are Lambertian for land and ice-covered surfaces and anisotropic (bidirectional) for water following the model by Minnis and Harrison (1984).

Clouds are inserted into the atmospheric model as horizontally and vertically (within one model layer) homogeneous layers. Mie theory is used for calculating the wavelength-dependent phase function for liquid water spheres and the doubling–adding method (Hansen and Travis 1974) is used to compute multiple scattering in clouds viewed from nadir. Scattering is azi-

TABLE 1. Absorbing and scattering components in each channel.

Component	Channel 1	Channel 2	Channel 3	Channel 4	Channel 5
H_2O	L	L	L, C	L, C	L, C
CO_2	L	L	—	L	L
O_3	C	C	—	L	L
O_2	L	L	—	L	—
N_2O	—	—	L	L	L
CH_4	—	—	L	—	—
N_2	—	—	C	—	—
Aerosols	I	I	I	—	—
Rayleigh scattering	I	I	—	—	—

Note: L: line absorption; C: continuum band; I: included.

muthally independent for nadir viewing geometry. Twelve Gauss points are used to account for varying solar zenith angles. The standard gamma distribution (Hansen 1971) is used for cloud droplet size distributions (see Appendix). This distribution agrees well with experimental data for stratus, altostratus, and fair weather cumulus (Hansen 1971), that is, low-level liquid water clouds. Note that throughout this paper, we discuss the cloud optical thickness in terms of its value at 0.6 μm; however, the actual value is wavelength dependent in all model calculations.

To illustrate the relative importance of cloud optical thickness, τ, effective droplet radius, r_e, and cloud-top temperature, T_C, on measurements at each AVHRR wavelength (see Appendix), we calculate radiances using the global average Standard Atmosphere profile, solar zenith angle = 60°, cloud optical thickness $\tau = 6$, cloud-top temperature $T_C = 270$ K (pressure $P_C = 720$ mb), and cloud droplet radius $r_e = 10$ μm. Cloud optical thickness is then varied from 0 to 50, r_e from 5 to 30 μm, T_C from 240 K to 284 K (P_C from 390 mb to 934 mb), and water vapor abundance from 123 cm STP to 2010 cm STP. Each quantity is varied separately; results are shown in Table 2 normalized to the largest effect for each channel. For example, to determine the r_e effect on channel 3 (solar reflectance), T_C and τ are set to typical values ($T_C = 270$ K and $\tau = 6$) and then r_e is varied from 5 μm to 30 μm to give a range of reflected solar radiances, ΔI_{reff}. Similarly, we get ΔI_τ and ΔI_{T_C} (with the typical r_e value as 10 μm). Normalized to the largest of ΔI_{reff}, ΔI_τ, and ΔI_{T_C}, we get the relative importance of each factor. The major effects of different atmospheric profiles are caused by differences in the water vapor abundance; however, since water vapor affects channel 1 and 3 radiances in the same direction, as discussed below, the relative effects are similar for all atmospheres.

TABLE 2. Relative importance of cloud properties in each AVHRR channel.

	T_C effect	r_e effect	τ effect
Channel 1	1.8	6.6	100
Channel 3 (solar reflection)	15.1	100	56.2
Channel 3 (thermal)	95.8	13.1	100
Channel 4	100	7.8	43.5

The "T_C effect" in channels 1 and 3 is actually caused by water vapor absorption, since changing T_C implies a change in the height of the cloud top and the amount of gas above the cloud. In channel 1 changing the amount of gas above the cloud alters the Rayleigh scattering contribution slightly; in channel 3 it changes the water vapor amount above the cloud and the consequent absorption. Only the water vapor above cloud absorbs 3.7-μm radiation observed by satellites because water clouds are strongly absorbing at this wavelength, so little sunlight reaches the water vapor below the cloud. The relative importance of τ variations on channel 3 solar reflectance is significant only for $\tau < 10$, because the channel 3 solar reflectance is limited by absorption at larger optical thicknesses (Han 1992); for τ greater than 10, the relative importance of τ is nearly zero. The results in this table show that a retrieval of cloud particle size from measurements at 3.7 μm requires accurate corrections for variations in the cloud optical thickness (at lower values) and cloud-top temperature (thermal emission and water vapor absorption).

c. *Retrieval scheme*

For a practical retrieval scheme that can be applied to every image pixel, we use lookup tables of precalculated radiances from the radiative transfer model to relate the measurements to cloud particle size. We use four lookup tables (a flow diagram of the retrieval scheme is shown in Fig. 1).

Starting with the ISCCP CX dataset, we select those AVHRR pixels that are determined to be cloudy by the ISCCP cloud detection procedure (Rossow and Garder 1993a). Because of difficulties with proper detection of clouds and retrieval of optical thicknesses over highly reflective surfaces at extreme solar zenith angles (e.g., Rossow et al. 1989; Rossow and Garder 1993b), we limit our analysis

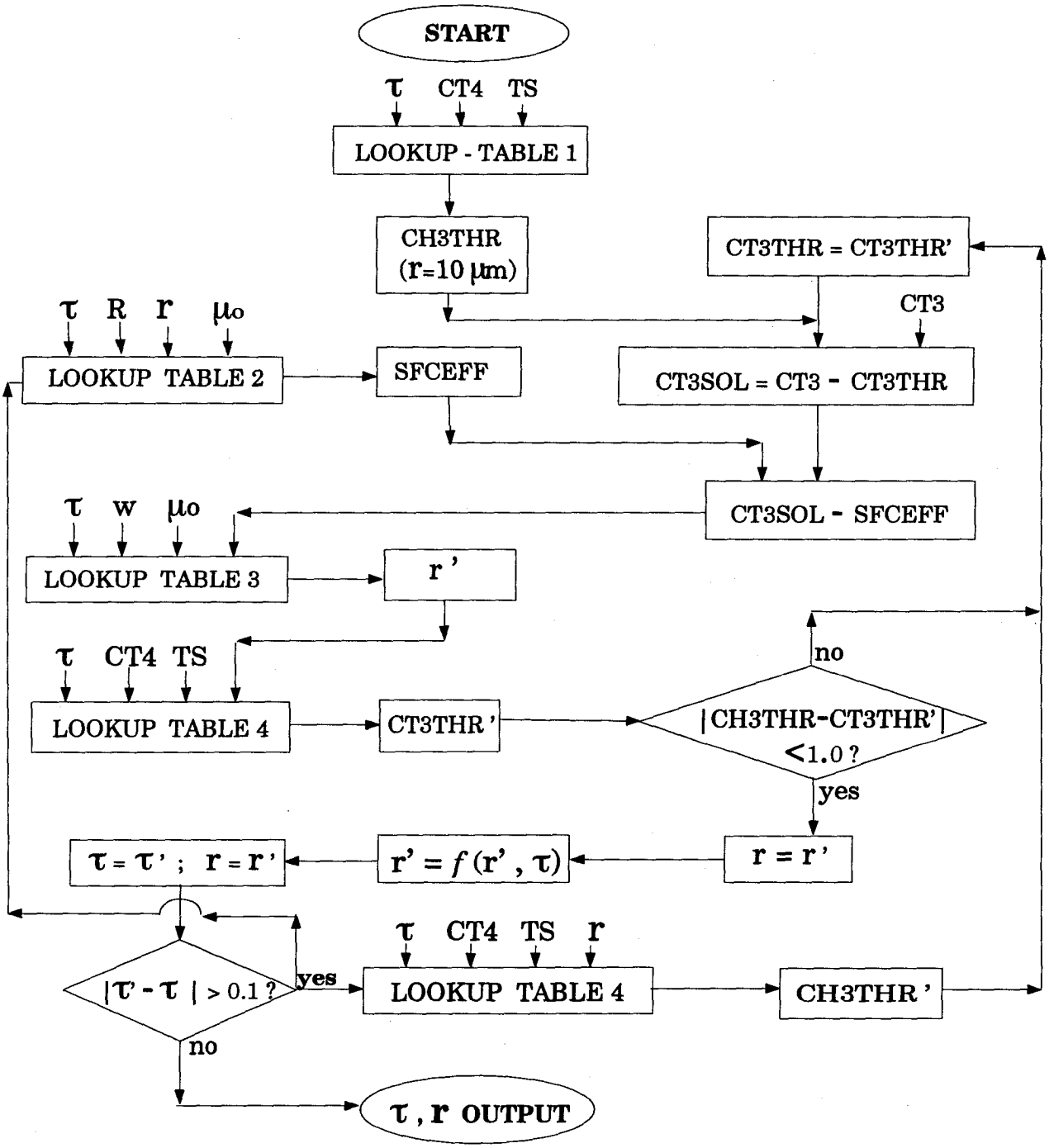

FIG. 1. Schematic of cloud droplet radius retrieval method.

to latitudes ±50°. To simplify the necessary radiative model calculations, this analysis is also limited to image pixels viewed near nadir for which the reflected radiation is independent of azimuth angle. The results show no dependence on cosine of the satellite zenith angle, μ, or azimuth angle, if we restrict its value > 0.9 [zenith angle < 26° (Han 1992)]. We select only liquid water clouds determined by $T_C > 273.2$ K.

The first lookup table is a first-guess value of the thermal emission contribution to 3.7-μm radiances (CT3THR in Fig. 1), using the ISCCP values of cloud optical thickness (τ), the assumed value of $r_e = 10$ μm, the channel 4 radiance (CT4), and the ISCCP surface

temperature (T_S) as entries. Because the cloud thermal emission is also a function of cloud particle size, we must start with the same particle size used in the ISCCP retrieval, 10 μm, in the first guess and iterate as improved values of r_e become available. Subtracting the estimated thermal emission from the total 3.7-μm radiance (CT3), we get the reflected solar radiance in channel 3 (CT3SOL).

The second lookup table removes the effect of solar radiation reflected from the surface (SFCEFF) to isolate the *cloud* reflectance at 3.7 μm. The magnitude of this effect depends on the cloud optical thickness. The table's inputs are cloud optical thickness (τ), cloud particle size ($r_e = 10$ μm as a first guess), surface reflectance for channel 3 (R_S), and cosine of the solar zenith angle (μ_0), where surface reflectance for a specific location is the monthly mean value derived from channel 3 measurements in clear pixels.

The third lookup table gives the cloud particle size, r', using entries for reflected solar radiance at 3.7 μm (CT3SOL–SFCEFF), the ISCCP cloud optical thickness (τ), cosine of the solar zenith angle (μ_0), and water vapor amount above the cloud (w) from TOVS and the cloud-top pressure. The new value of cloud droplet radius (the second guess) is entered into the fourth table (Table 4 is the same as Table 1 for $r_e = 10$ μm) to obtain an improved estimate of the cloud thermal emission at 3.7 μm (CT3THR′). If the difference between this new value and the previous (or first) guess (CT3THR) is larger than one count number (about 0.5 K), we subtract the new value of the thermal emission contribution from the 3.7-μm radiance and repeat the whole particle size retrieval (the calculation of SFCEFF is also repeated). This process continues until CT3THR′ equals CT3THR. Then $r_e = r'$ is the effective radius for $\tau = \tau_0$ (τ_0 is cloud optical thickness retrieved by ISCCP assuming r_e equals 10 μm).

Next, the effect of particle size on cloud optical thickness is accounted for by an iterative calculation that includes changes in cloud optical thickness in the retrieval. Two cloud layers have about the same reflection, transmission, and absorption properties if they have the same values for a scaled optical thickness and scaled single-scattering albedo (van de Hulst 1980; Twomey et al. 1984). The similarity equation

$$\tau'(1 - \tilde{\omega}_0' g') = \tau(1 - \tilde{\omega}_0 g) \qquad (1)$$

is used to get τ' from τ and r' ($\tilde{\omega}_0$ and g are functions of wavelength and droplet radius and are calculated using Mie theory and the optical constants of liquid water; see Table 1 in the Appendix, instead of using the scaling equations for these quantities). If the difference of τ' and τ is greater than a threshold value, discussed below, the fourth lookup table is used again to get a new CT3THR′ and the whole r_e retrieval repeats until τ converges (the calculation of SFCEFF is also repeated in each cycle).

The primary consideration in choosing convergence criteria for τ is computer time and the magnitude of errors. The iterative process is terminated if the difference of retrieved particle sizes in two successive cycles is $|r' - r_e| \leq 1$ μm (which is within the estimated accuracy of the retrieval scheme) and $|\tau' - \tau| < 0.1$ (this is the smallest interval in ISCCP values of τ). With these criteria, the data processing speed and the error are satisfactory (Han 1992).

4. Sensitivity tests and verification

a. Radiative transfer model consistency and sensitivity checks

The basic aspects of the radiative transfer physics have been described in many previous studies (e.g., Hansen and Travis 1974; Lacis and Hansen 1974; Liou 1980; Goody and Yung 1989; Lacis and Oinas 1991) and some specific results of applications to clouds have been checked (e.g., King and Harshvardhan 1986; Rossow et al. 1987; Takano and Liou 1989; Rossow et al. 1989; Kobayashi 1993). We have checked the consistency of the radiative transfer model by determining whether the observed range of radiances, particularly in channels 3 and 4, can be described by the model with surface, atmosphere, and cloud parameters within a reasonable range. These comparisons show that clear radiances calculated by the model are consistent with independently determined values of water vapor abundance and surface temperature. Cloudy radiances can be matched by variations of cloud optical thickness and particle size that are well within the range of other estimates (Han 1992).

We investigated the uncertainty associated with removal of the thermal radiation and the surface solar reflectance contributions to channel 3 radiances by sensitivity studies that varied these parameters systematically over the whole range of observed values. For clouds with $r_e < 20$ μm and $\tau > 1.0$, a 10% variation in the thermal emission contribution to channel 3 radiances (for example, a channel 4 scene brightness temperature uncertainty of about 4 K at about 270 K with solar illumination from a zenith angle of 60°) changes the retrieved value of r_e by < 0.7 μm. For clouds with $r_e \sim 40$ μm or larger, reflected solar radiance in channel 3 is almost independent of droplet radius because of the strong absorption of liquid water at 3.7-μm wavelength (cf. Nakajima and King 1990). Hence, our retrieval cannot distinguish among liquid water droplets larger than about 40 μm in radius.

The effects of surface reflectance uncertainties are largest for low optical thickness clouds over land. Sea surface reflectance for channel 3 is specified as Lambertian with value of 2.5%, consistent with measured values obtained from 1 month of clear-sky radiances viewed at nadir. Over land for each month, we use all the clear-sky pixel radiances to construct a map of monthly mean channel 3 surface reflectance. The dis-

tribution of observed land surface reflectances covers the range from 5%–20%. A 5% (absolute) variation in surface reflectance alters the retrieved values of r_e in a cloud with $\tau \sim 1$ by <0.3 μm; the effect is proportionately larger for lower values of τ and is completely negligible for $\tau > 3$ (Han 1992).

When both τ and r_e are small, multivalued solutions are encountered (cf., Nakajima and King 1990; Han 1992). Because of a larger imaginary refractive index for liquid water at 3.7 μm ($\sim 3.55 \times 10^{-3}$ compared with 2.72×10^{-4} at 2.2 μm and 7.89×10^{-5} at 1.6 μm), this problem occurs at smaller values of τ (cf. Fig. 2) than at 2.2- and 1.6-μm wavelengths. Hence, for $\tau < 3$ and $r_e < 4$ μm, we cannot obtain unique retrievals and the results are discarded [the corresponding cutoff value of τ at 2.2-μm wavelength is about 12 (cf. Fig. 2 of Nakajima and King 1990)].

We also tested the effect of the satellite zenith angle restriction by determining at what value the shapes of the retrieved r_e distributions begin to change shape. These results show no changes in the shape or average r_e values for satellite zenith angles <26° (Han 1992).

b. *Retrieval scheme tests*

A direct test of the retrieval scheme precision is to compare its results with detailed radiative transfer calculations. We used the model to calculate channel 3 and 4 radiances for a wide range of μ_0 (solar zenith angles 0°–76°), τ (0.3–30), atmospheric profiles (global mean, Tropics, midlatitude summer, midlatitude winter from Standard Atmosphere), P_C (255 mb–934 mb), and r_e (5, 10, 20, 30 μm). Then, these radiances, together with the same solar zenith angle, τ_0 (τ for $r_e = 10$ μm) and atmosphere and surface properties, are entered into the retrieval scheme as synthetic observations and values of r_e and τ retrieved. Comparison of the values of τ and r_e used to calculate radiances with the values retrieved from the radiances shows that the retrieved results are systematically smaller by 0.2–0.3 μm with standard deviations ranging from 0.7 at 5 μm to 2.9 μm at 30 μm (corresponding to 15% errors at the smallest sizes to 10% errors at the largest sizes).

c. *Effect of partial cloud cover*

To calculate radiances for individual satellite image pixels, we assume a uniform, plane-parallel cloud layer in the radiative transfer model; but many clouds are broken (partial coverage) on spatial scales near or below the size of satellite radiometer fields of view (Coakley and Bretherton 1982; Harshvardhan 1982; Coakley and Baldwin 1984; Davies 1984; Welch and Wielicki 1989; Wielicki and Parker 1992; Chang and Coakley 1993). These "cloud cover" variations can also be thought of as optical thickness variations, where zero is just one value in the distribution (Rossow 1989). In fact, whether they are broken or not, clouds exhibit variations in all their properties on all scales (cf. Prup-

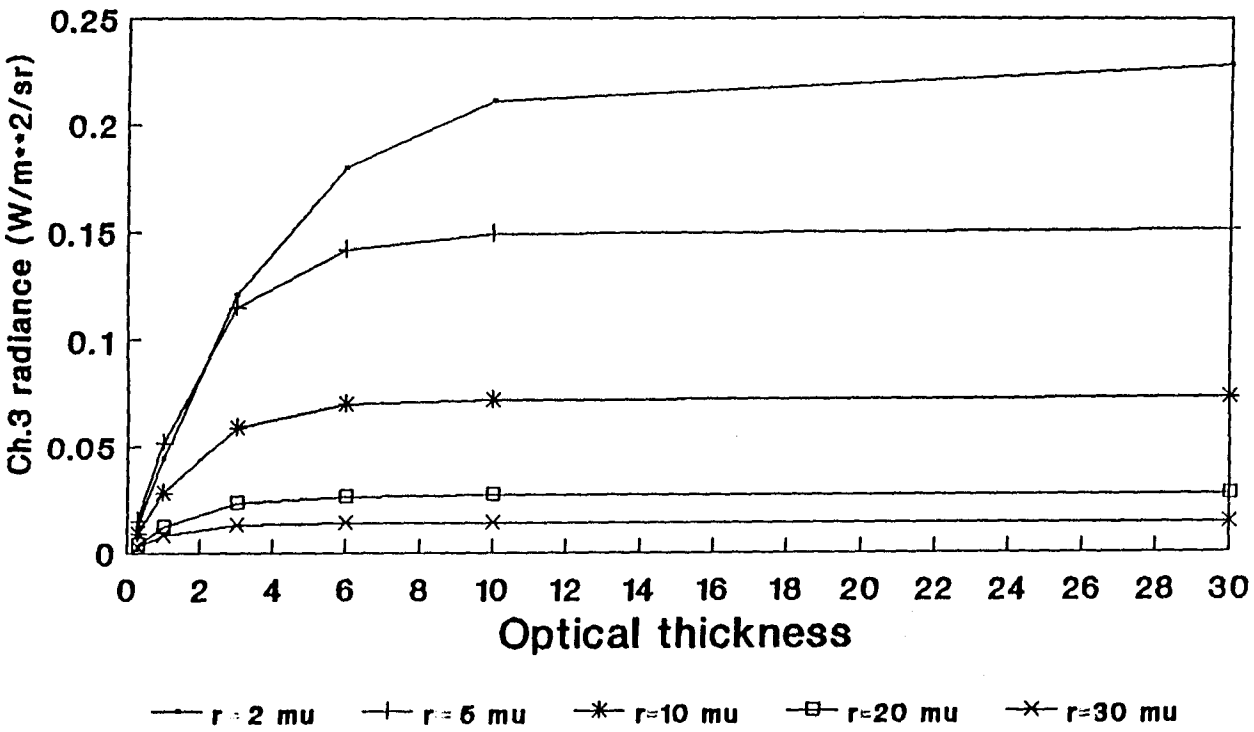

FIG. 2. Variation of AVHRR channel 3 (3.7 μm) radiances with cloud optical thickness for different water droplet effective radii.

pacher and Klett 1978), including both optical thicknesses (Wielicki and Parker 1992) and cloud particle radii (Coakley 1991). All of these small-scale optical property variations, including cloud shapes, affect the radiation scattered and absorbed by clouds (cf. Davies 1978; Welch and Wielicki 1984; Coakley and Davies 1986; Coakley and Kobayashi 1989; Kobayashi 1993), although most studies concentrate on the variation of a single parameter.

Comparison of the ISCCP and surface-based cloud climatologies (Warren et al. 1986, 1988) suggests that the frequency of broken cloudiness on scales smaller than about 50–200 km is about 20%–30% (Rossow et al. 1993); however, we do not have an accurate enough idea of the size distributions of broken cloud types to estimate the frequency of partial cloud cover for areas as small as the AVHRR pixels. Chang and Coakley (1993) suggest, based on a comparison of threshold and spatial coherence cloud amounts for 8×8 km^2 areas, that this frequency can be as large as 50% for marine stratocumulus clouds; however, Wielicki and Parker (1992) show evidence that this estimate is too high by almost a factor of 2 because the spatial coherence method interprets all radiance variations to be caused by subpixel cloud cover variations when significant radiance variation is also caused by optical thickness variations. Thus, although rms errors of cloud amount in individual pixels are as large as 20%–30% for 8-km pixels (Wielicki and Parker 1992), with similar errors in optical thickness implied, random errors are <10% for 4×1 km^2 areas and average errors in the *mean* cloud amount and optical thickness are only a few percent for marine boundary-layer cloudiness when using the ISCCP thresholds (Wielicki and Parker 1992).

Studies of the angular dependence of visible radiances from various cloud types suggest systematic differences with the plane-parallel representation that affect the retrieved value of optical thickness (Davies 1984; Coakley and Kobayashi 1989; Kobayashi 1993). Similar effects have been shown at 3.7 μm, where they are attributed both to shape effects and to systematic variations of cloud particle size within clouds (Coakley and Davies 1986; Coakley 1991). Most of these studies have focused on the direct effects of small-scale variations on cloud albedos rather than on the effects of retrieval of cloud properties from radiances. Using a more appropriate Monte Carlo model, Kobayashi (1993) shows that the cloud albedo calculated from the optical thickness retrieved from a visible radiance using a plane-parallel and homogeneous model does not differ by more than 10% from the actual albedo of broken clouds except when the retrieval is performed at too large satellite and solar zenith angles. For our near-nadir analysis, negative biases in the optical thicknesses are estimated to be much less than 10%; however, somewhat larger positive biases may occur at large solar zenith angles.

Given the small-scale variations of all the cloud properties, the values of τ and r_e that we retrieve must be thought of as radiatively weighted averages over a finite cloud domain: these parameters are a single combination of values that best represent the observed radiances. To provide a crude estimate of the sensitivity of our retrievals of r_e to the effects of subpixel cloud variations, we resort to the calculation of the satellite-received radiance from a partially cloudy pixel by

$$F = (1 - f)F_s + fF_c, \tag{2}$$

where f is the fractional cloud cover, F_s is the radiance associated with the cloud-free portion of the field of view, F_c is the radiance for the overcast portion, and the cloudy and clear portions are treated as plane parallel. This approach puts all of the variability into cloud cover, so it is probably an upper limit (cf. discussion in Kobayashi 1993). Channel 1 and channel 3 reflectivities are calculated using (2) for a satellite zenith angle of 0°, a solar zenith angle of 60°, $\tau = 30$, $r_e = 10$ μm with variable cloud cover fractions, as well as for overcast conditions, and variable cloud optical thicknesses from 0 to 30.

Figure 3 shows the retrieved values of cloud optical thickness and cloud particle radius as a function of the assumed subpixel cloud cover. For this particular viewing geometry, a channel 1 reflectivity of 0.23, for example, would be interpreted as a cloud optical thickness, $\tau = 5$, assuming overcast conditions, and the corresponding channel 3 reflectivity would be interpreted as $r_e = 18$ μm. The same radiance, however, could be due to reflection from a broken cloud system with $\tau = 30$, $r_e = 10$ μm, and cloud fraction $f = 0.34$. Note that the relative magnitude of the effect of subpixel cloud cover on τ is much larger than on r_e because the former depends directly on the magnitude of the re-

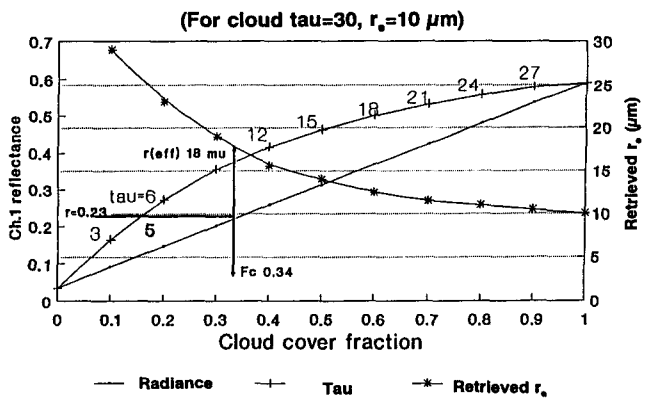

FIG. 3. Variation of AVHRR channel 1 (0.6 μm) reflectances (line with dots and curved line with +, left scale) and the retrieved value of the water droplet effective radius (curved line with *, right scale) with the fraction of the image pixel covered by cloud. The reflectance curve labeled with values of cloud optical thickness (tau) shows the corresponding reflectances for clouds with 100% cover but varying optical thickness.

flected channel 1 radiance while the latter depends on the difference (or ratio) of two reflected radiances. Note also that the overcast pixel assumption causes an overestimate of r_e and an underestimate of τ for broken clouds. The typical overestimate of cloud cover caused solely by the finite field of view has been estimated to be about ~10% for the AVHRR pixel size (Wielicki and Parker 1992; Chang and Coakley 1993), which implies a potential bias in our retrieved cloud droplet radii of, at most, about 1 μm. However, the actual situation is more complicated because optical thicknesses and particle size variations may be correlated with the variations of cloud cover.

d. Cirrus contamination

Although we exclude all clouds with $T_C < 273$ (where the T_C values have been corrected for transmission of IR radiation from below using the measured optical thicknesses), this criterion does not prevent some observations being composed of a very thin, high-altitude cloud (presumably composed of ice) overlying a lower-level water cloud. Since the 3.7-μm absorption signature is dominated by the upper part of the cloud (as we show), contamination by thin cirrus would mix the properties of the ice and water clouds in the retrieval of particle size. We use model calculations to examine the possible effects of cirrus contamination. Figure 4 shows the retrieved droplet radius and cloud brightness temperatures for two-layer cloud systems, for midlatitude summer atmospheric conditions, each with a high cirrus cloud at a temperature of 231 K containing spherical ice crystals with r_e = 30 μm [which corresponds to a liquid water droplet radius of ~38 μm if the retrieval is performed assuming the refractive index of liquid water (see Fig. 5)] and a low-level liquid water cloud at a temperature of 291 K with r_e = 10-μm droplets. The total optical thickness of the two clouds is held fixed at τ = 6 and the optical thickness of the cirrus layer is varied from 0 to 2 (the low cloud τ decreases accordingly). The observed brightness temperature of channel 4, TB4, decreases monotonically as τ_{cirrus} increases. For these conditions, values of TB4 > 273 K occur when $\tau_{\text{cirrus}} < 1$; the largest retrieved value of r_e occurs for a cirrus cloud with τ = 1, in which case $r_e \sim 22$ μm.

Figure 4 also shows that the retrieved cloud particle radius converges to that of the upper cloud value when its τ reaches about 2. In other words, information about particle size comes from the uppermost optical thickness, less than or about 2, at the cloud top. Thus, even if a very different microphysics exists below the τ = 2 level from the top of cloud (in this case, $r_e \doteq$ 10-μm water spheres under r_e = 30 μm ice spheres), it will have little effect on the retrieved particle size even though this material contributes to the total optical thickness. This fact also affects comparisons of satellite retrievals with in situ measurements of droplet radii

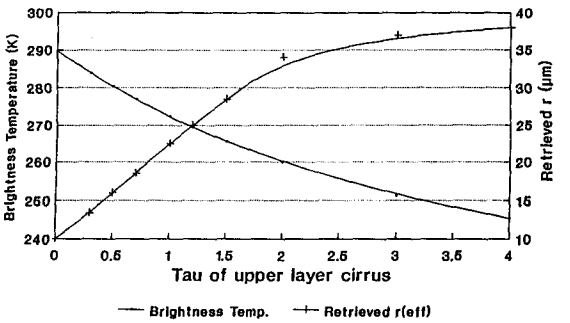

FIG. 4. Variation of AVHRR channel 4 (10.5 μm) brightness temperature (line with dots, left scale) and the retrieved water droplet effective radius (line with +, right scale) with the optical thickness of an upper cirrus cloud layer, composed of ice spheres with an effective radius of 30 μm, overlying a water cloud with droplet effective radius = 10 μm. Total column optical thickness is fixed at 6.

by aircraft instruments if there is vertical variation of cloud droplet size (cf. Nakajima et al. 1991).

We test the extent of cirrus contamination in our results in two ways. First, we compare the shape of the distributions of r_e obtained from many clouds with two different T_C thresholds, 273 K and 280 K. Figure 4 shows that the higher threshold decreases the possible effect of cirrus contamination on r_e by about a factor of 2. If the r_e distribution shapes were significantly altered by this change, then our results would be significantly contaminated. We limit the comparison to maritime clouds to avoid confusion with the effects of strong vertical gradients in cloud condensation nuclei that occur over land (see section 5a). There do not appear to be large differences in cirrus cloud amount between land and ocean (Warren et al. 1986, 1988; Wylie and Menzel 1991). Figure 6 shows some sample distributions of r_e retrieved with the two T_C thresholds in different latitudes and months; the thick lines are for $T_C \geq 280$ K and the thin lines are for $T_C \geq 273$ K. Also shown in the upper-right corner of each panel are the number of pixels and the mean values of r_e for the two thresholds. Although there are small changes in the distributions at the largest radii, which might indicate cirrus contamination, there is no systematic effect on the overall distribution shapes or on the mode and mean radii. Only 3%–6% of the retrievals indicate droplet radii >40 μm that might be caused by cirrus contamination. If we attribute all of the changes produced in this test to cirrus contamination, the largest observed effect (e.g., July 1987 at 30°S to 40°S) is an increase in the mean effective radius of about 1 μm.

Secondly, we compare the geographic distribution of the average values of r_e with that of cirrus cloud amounts for the same months (January, April, July, and October) from surface observations (Warren et al. 1986, 1988), and from the ISCCP climatology (Rossow and Schiffer 1991) to see if there is any correspondence between the occurrence of large r_e (>15 μm) and larger

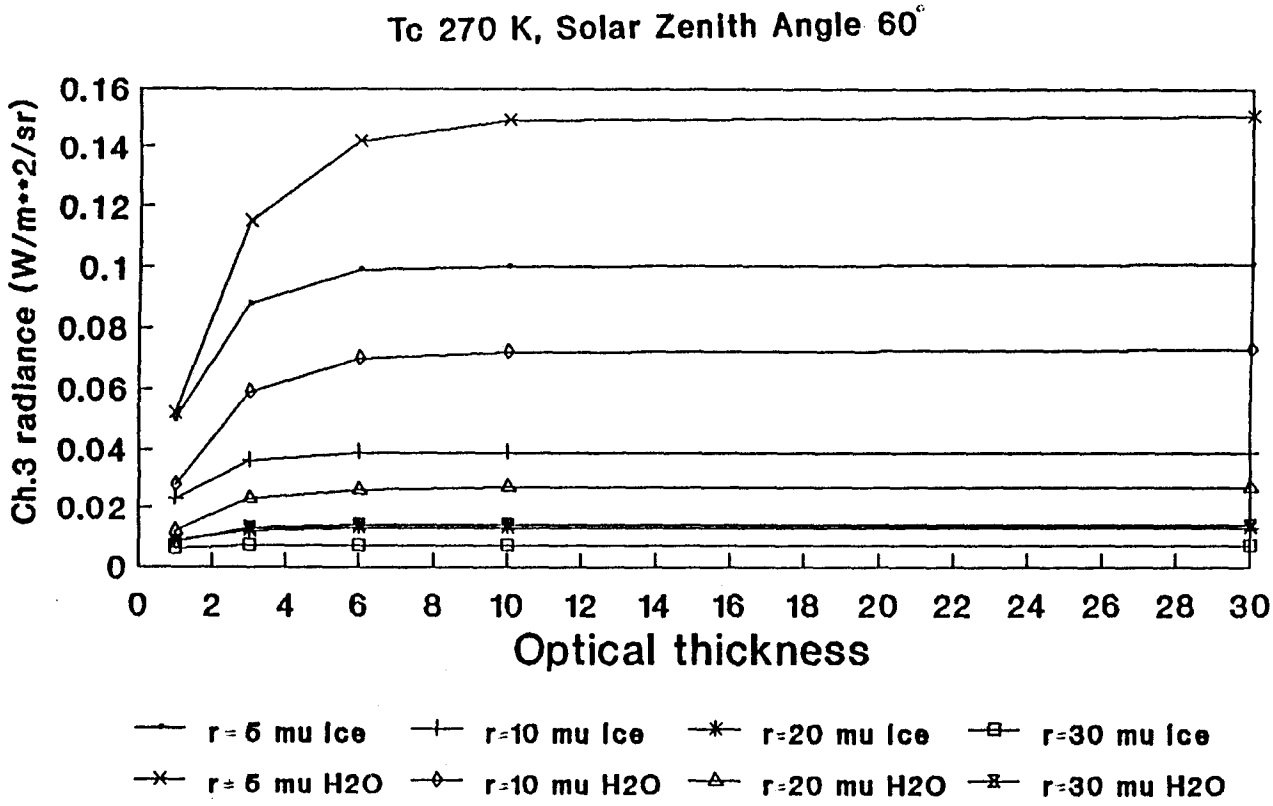

FIG. 5. Variation of AVHRR channel 3 radiances with cloud optical thickness for water and ice spheres with different effective radii. Cloud-top temperature, T_C, and solar zenith angle are specified as shown.

cirrus amounts. For example, in January, large cirrus amounts occur over the equatorial central Pacific, the Indonesian islands, central South America, and central Africa, but none of these regions shows r_e values larger than elsewhere in the tropics (cf. Fig. 11). On the contrary, the largest particle sizes occur in regions over the southern Indian Ocean, South Atlantic Ocean, and southeast Pacific (Fig. 11) that are associated with the lowest cirrus amounts. The only regions that show some correspondence between large r_e and large cirrus amounts are in central Asia in April 1987 and in the western U.S. Rocky Mountains in January 1987. The ISCCP climatology shows 40% to 60% cirrus amount and our results show droplet sizes as large as 18 μm. A similar effect is noticeable over some small portions of the wintertime continents in the Northern Hemisphere. Thus, cirrus (or ice cloud) contamination may be affecting our results over high topography and in some winter continent locations.

Figure 5 suggests an explanation for a few other instances of much larger r_e values that occur near a few specific coastal areas, especially if very low optical thickness ($\tau < 1$) clouds are isolated. These locations, off the east coasts of North America and Asia in summer and off the west coast of tropical North Africa, especially in summer, are known to be regions of very large aerosol abundance, the former associated with human pollution sources and the latter associated with dust storms. If these cloud particles are not composed of liquid water as assumed in the radiative model, but are formed from a more absorbing substance (both sulfuric acid and silicates are stronger absorbers at 3.7 μm), then the retrieved r_e will be large, even if the actual particle size is small, to account for the absorption. Figure 5 shows this effect on the 3.7-μm radiances by comparing liquid water and ice spheres of the same size, where the liquid water is less absorbing so that larger particle sizes are required to match the observed ratio of 3.7-μm absorption and 0.6-μm scattering. Test retrievals for a few cases in these locations, using the refractive index of silicate dust and sulfuric acid, reduce r_e values to 2–5 μm from 15–20 μm when treated as liquid water.

e. Comparison with in situ measurements

The viewing angle constraint in our analysis limits the area covered by the radiometer in each overflight of a particular region; thus, we do not find many precise matches in time and location with the few published FIRE (First ISCCP Regional Experiment) measurements (e.g., Rawlins and Foot 1990; Radke et al. 1989;

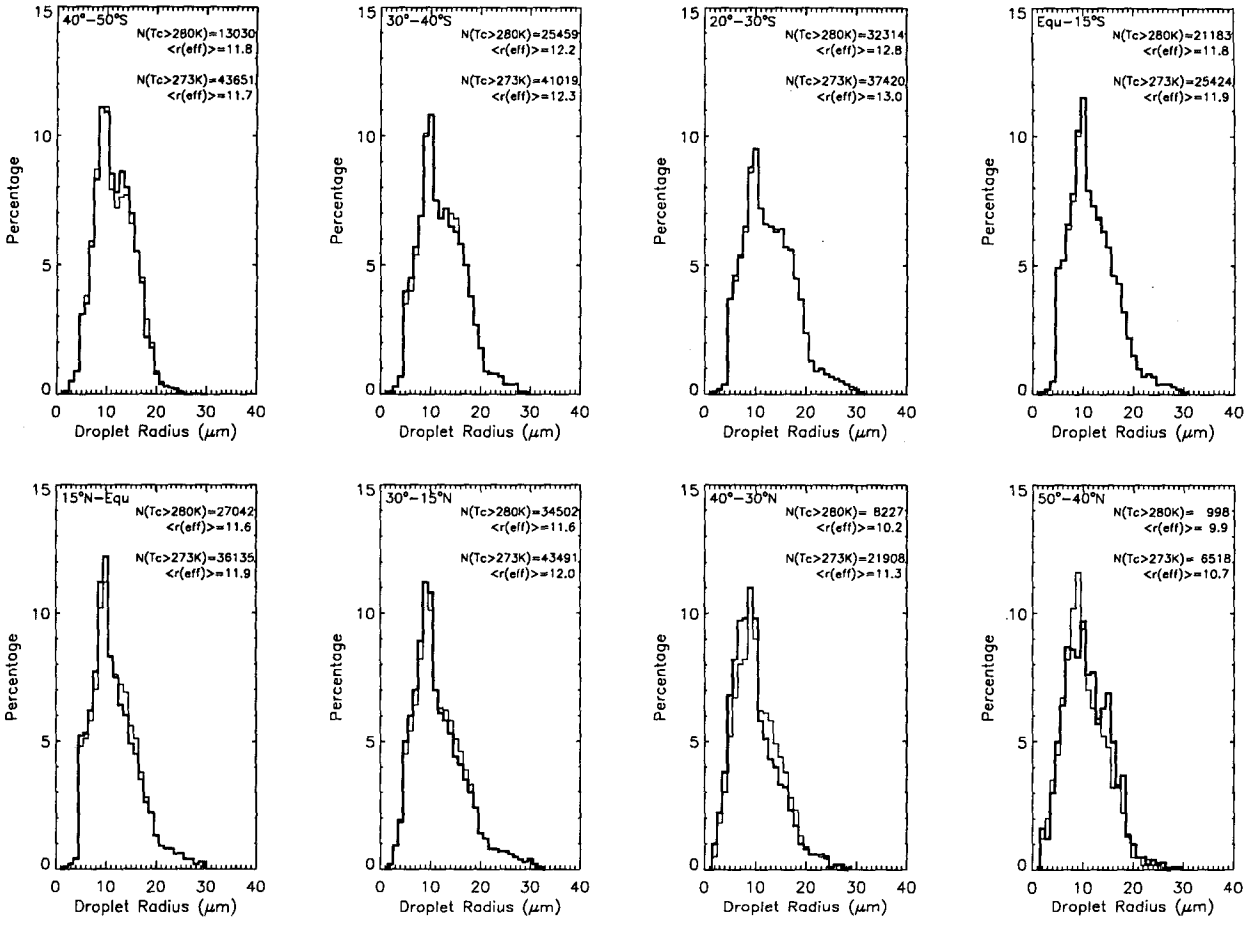

FIG. 6. Distributions of the frequency, N, of cloud droplet effective radius values in different latitude zones over the global ocean for (a) January and (b) July 1987 retrieved with two different thresholds of cloud-top temperature, $T_C > 280$ K and $T_C > 273$ K. The average over the distributions is shown as $\langle r(eff) \rangle$ in microns.

Nakajima et al. 1991). The results of Nakajima et al. (1991) are the best match in location and time. Moreover, their results compare an analysis of radiance measurements from the high-altitude aircraft (NASA ER-2), similar to a satellite retrieval, with matched in situ measurements from a lower-altitude aircraft in the cloud. The published results include measurements for 7, 10, 13, and 16 July 1987, in the region 30.8°N to 32.0°N and 120.1° to 122.2°W around 1100 local time (each measurement lasts ~10 min). The *NOAA-9* crossing time in this area is approximately 1418 local time (2218 UTC), but the nadir track passes through the target area only on 7 and 16 July, although we collected satellite data for a larger region: 117.0° to 122.0°W and 30.8°N to 32.0°N.

Figure 7 is modified from Fig. 10 of Nakajima et al. (1991) by superimposing our results for comparison (dashed lines are their results and solid lines are ours). The contours represent the frequency of occurrence of each optical thickness—droplet radius pair. Table 3 compares mean and standard deviation values. The general features of the relationship between droplet size and optical thickness are very similar in both results and change in the same way from one day to the other. Our results show slightly larger droplet radii on the 16th and slightly smaller optical thicknesses on both days: the range in both quantities is also larger in our results on 16 July.

Nakajima et al. (1991) indicate that their retrieved particle sizes are larger than those determined from in situ measurements by 2–3 μm; however, their retrieved values may be too large because of an underestimate of atmospheric absorption in their radiative model (Taylor 1992). As we show (Table 7), there is also a systematic diurnal variation in cloud optical thickness and droplet size in marine stratus such that our results from later in the day should exhibit somewhat smaller values of τ and slightly larger values of r_e. The comparison in Table 3 and Fig. 7 is consistent with this expectation, if the r_e values from Nakajima et al. (1991) are assumed to be slightly too large. We note that this comparison

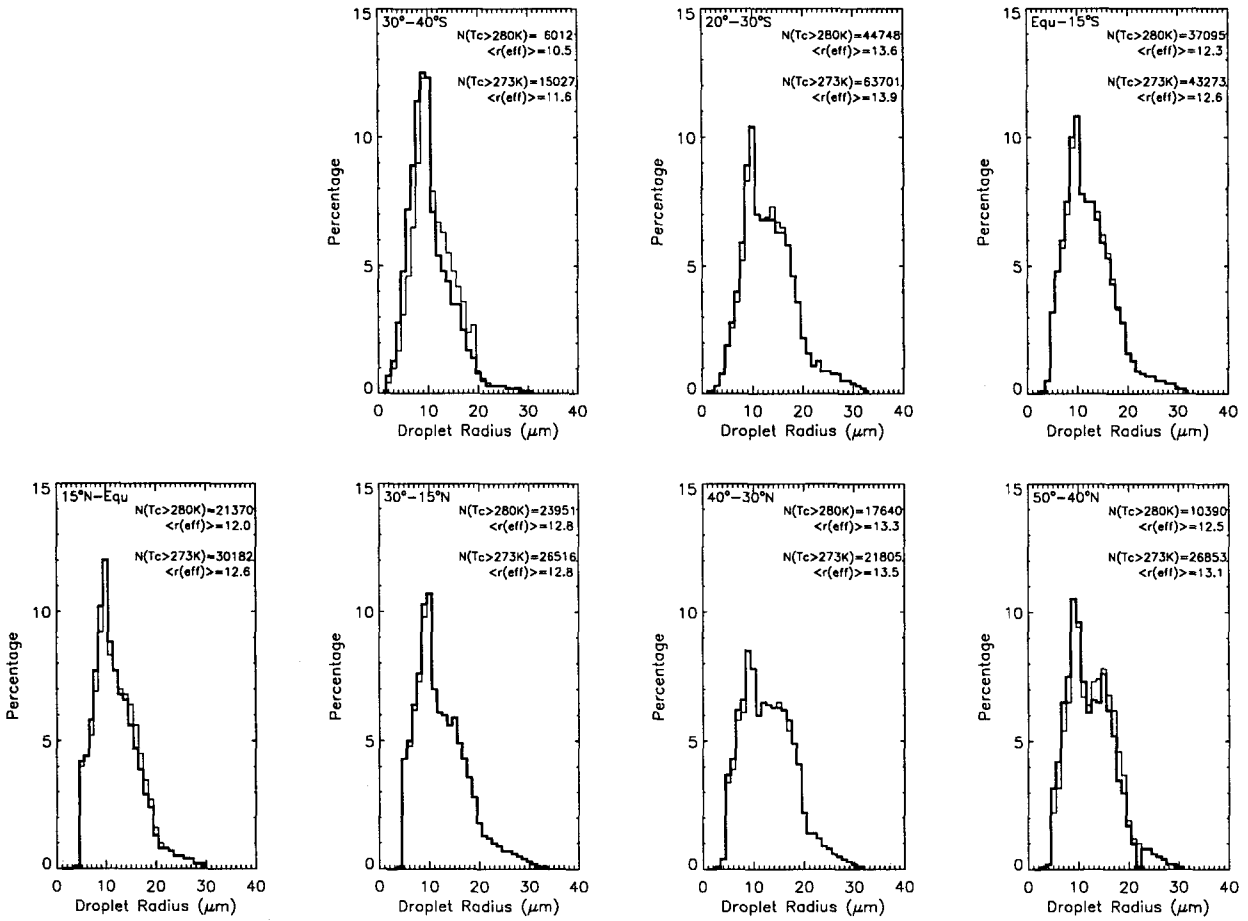

FIG. 6. (*Continued*)

does not indicate any large bias that may be associated with broken cloud effects, but many more comparisons are needed to be sure.

Minnis et al. (1992) also infer effective droplet radii for marine stratus clouds observed during FIRE from a completely different set of measurements: they combine cloud optical thickness values retrieved from satellite-measured visible radiances with liquid water path values obtained from collocated microwave radiances measured from San Nicholas Island. There are nine matches with our results (Table 3): the Minnis et al. values are, on average, about 1 to 1.5 μm larger than ours with an rms difference of about 2.5 to 3.5 μm (depending on whether we interpolate between Minnis et al. values or pick the nearest match in time). Minnis et al. (1992) also show a mean diurnal variation of droplet radii: the maximum value is about 13 μm just after sunrise and falls to a minimum of about 5 μm in midafternoon. Our average droplet radii from *NOAA-10* (overflight at about 0730 local time) and *NOAA-9* (overflight at about 1515 local time) are about 11 and 9 μm, respectively.

f. Summary of uncertainties

1) RANDOM UNCERTAINTY

The observed width of the distribution of retrieved cloud droplet radii consists of two components: real variability in r_e and random retrieval errors. The latter includes random uncertainties due to radiance noise, neglected atmospheric and surface variability, and part of the effects of cloud morphology variations. Therefore, an upper limit on the random retrieval uncertainty can be set by the narrowest observed cloud droplet radius distribution we can find. One of the more homogeneous cloud types is the large subtropical marine stratus cloud decks off the west coasts of the continents. Table 4 illustrates the general results for all marine stratus regimes with the mean radii and standard deviations observed for an area off the California coast (30°–35°N, 120°–125°W). Observations from FIRE show fluctuations of the cloud effective droplet radius between 18 and 6 μm within a 150-km aircraft flight track (Fig. 3 of Nakajima et al. 1991). We find narrower distributions farther from the coast in October

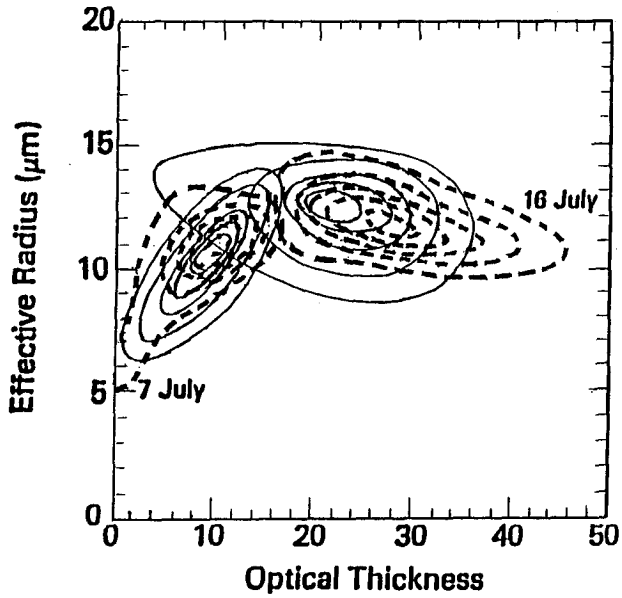

FIG. 7. Comparison of joint frequency distributions of retrieved cloud droplet effective radii and cloud optical thicknesses obtained from FIRE aircraft measurements (Nakajima et al. 1991) on 7 and 16 July 1987 (dashed contours) and from this analysis of *NOAA-9* AVHRR data for the same dates and location (solid contours). Frequency contours represent, from outer to inner, 10%, 30%, 50%, 70%, and 90% of the peak value.

of 1987. The standard deviations of these measurements are 1–2 μm, which suggests that the random uncertainty, directly attributable to our retrieval method, is no more than this amount (Table 4). Somewhat larger sources of error, discussed below, may cause larger "random" errors too. We conclude that the larger dispersion of r_e values in our results (cf. Fig. 6) represents real variability among clouds. The consequent uncertainty in monthly mean values of r_e is less than 0.1 μm since the typical number of observations in a single map cell is about 100 per month.

2) BIASES

We have made rough estimates of the biases that may be produced by the effects of partial cloud cover in image pixels and by cirrus contamination. Both of these effects cause positive biases, but it is difficult to quantify these effects globally without a large number of comparisons to simultaneous in situ measurements in different meteorological regimes. The comparison with in situ FIRE results suggests that our values might be biased by 1–2 μm, but the comparison with other remote sensing analyses produces contradictory results for the sign of this bias.

During the initial formation stage of a cloud, when vapor condensation predominates and particle growth by collision has not yet begun, the clouds may exhibit a nearly uniform cloud droplet size of about 7 μm (Goody and Walker 1972). Aircraft measurements performed during FIRE in July 1987 (Fig. 3 in Nakajima et al. 1991) show varying mean droplet radii along the flight track with a minimum value of 6 μm observed over a path more than 50 km long. We examined our results for this same time and region and found many such uniform (standard deviations of r_e about 1 μm) regions >100 km across with effective droplet radii of 6 μm. Since the marine stratus cloud regime is characterized by frequent broken cloudiness with very small cloud elements, but generally devoid of cirrus clouds (Warren et al. 1988), this observation provides circumstantial evidence that any bias in our retrievals due to smaller-scale variations must be less than or of order 1 μm.

Cirrus cloud contamination does not appear to be a serious problem, except in some specific locations over mountains and over wintertime continents at the highest illuminated latitudes; however, a pervasive global coverage by very thin cirrus could introduce biases of 1–2 μm without leaving any particular signature. Thus, more comprehensive comparisons with in situ measurements are required to reduce this source of uncertainty in satellite-based measurements of cloud particle sizes.

TABLE 3. Comparison of satellite [MHYFS = Minnis et al. (1992)] and aircraft [NKS = Nakajima et al. (1991)] inferences of cloud properties in marine stratus clouds from FIRE, July 1987. The NKS results are for a region 30.8°N to 32.0°N and 120.1° to 122.2°W at around 1100 local time; our results are for the same latitude range and 117.0° to 122.0°W longitude at about 1415 local time. The matching dates between MHYFS and our results are 4–9 and 14–16 July 1987. All values are in microns.

	Mean droplet radius (standard deviation)	Mean optical thickness (standard deviation)
NKS (7 July)	10.9 (1.1)	10.0 (3.3)
This result	10.4 (1.7)	9.2 (3.1)
NKS (16 July)	11.7 (1.0)	27.8 (6.7)
This result	12.4 (1.2)	22.5 (6.2)
MHYFS	10.8 (4.1)	
This result	10.1 (3.2)	

TABLE 4. Mean and standard deviations from cloud radius distributions for October 1987 for 30°–35°N, 120°–125°W. *N*: number of pixels.

	Cloud $\tau \geq 6.0$		All cloud τ	
Date	$r_e + \sigma$ (μm)	*N*	$r_e + \sigma$ (μm)	*N*
06	6.6 ± 1.3	30	6.0 ± 1.4	107
07	7.0 ± 1.1	360	6.9 ± 1.2	423
08	6.6 ± 1.2	263	6.7 ± 1.3	290
15	7.9 ± 1.9	280	7.5 ± 2.1	319
16	7.4 ± 1.7	360	7.1 ± 1.9	412
17	7.3 ± 1.5	196	7.0 ± 1.7	235

5. Near-global survey of particle size in liquid water clouds

We have analyzed the AVHRR data from the *NOAA-9* ("afternoon") and *NOAA-10* ("morning") orbiters for January, April, July, and October 1987 and 1988 for latitudes between 50°N and 50°S (about 77% of earth's surface area). We define an "annual" average to be the average of these four months and a "global" mean to be the average over 50°N to 50°S. In the figures open symbols (circle, square, triangle, etc.) represent maritime clouds and filled symbols represent continental clouds. Note that since we limit our analysis to clouds with $T_C > 273$ K, the wintertime sample at higher latitudes is quite limited.

The droplet size distribution in a liquid water cloud is controlled by an approximate balance of microphysical processes. In the case of a nonprecipitating cloud, growth of droplets by condensation balances the supply of supersaturated vapor produced by ascending motions soon after cloud formation begins; but this balance may be affected by sedimentation of the larger droplets and evaporation of droplets when environmental air is mixed into the cloud later in the growth stage. The latter processes continue to erode the droplet size distribution when the ascending motions cease and the cloud decays. In a precipitating cloud (no ice phase), collisional growth of droplets supersedes condensational growth and is balanced by sedimentation of the precipitation. Comparison of the rates of change of mean (mass weighted) droplet radius caused by these processes with the typical lifetime of a nonprecipitating cloud indicates that their droplet radii should be about 5–15 μm. If the droplets were much larger, collisional growth would become important. The interaction of condensation, collision, and sedimentation in a precipitating cloud should produce cloud mean droplet radii of 10–30 μm [see Rossow (1978) for a discussion of such estimates]. Although even larger droplets are produced by collisional growth, these "precipitation-sized" droplets are quickly removed from the cloud, so that the cloud-mean droplet radius will remain above but near the value at which collisional growth rates significantly exceed condensational growth rates, which is about 10–20 μm. Thus over the earth, the typical value of the (mass weighted) mean droplet radius in liquid water clouds should be in the range 5–30 μm.

Droplet radii inferred from radiation measurements are cross section weighted, so that the mean effective droplet radii should be somewhat smaller than the mass-weighted values. Thus, our globally and annually averaged value of the effective droplet radius for liquid water clouds, 11.4 ± 5.6 μm, is completely consistent with microphysical theory and does not indicate a large bias in the analysis. Although the sensitivity of the 3.7-μm radiances to droplet radius is limited to the range of about 2–35 μm, the distribution of our results shows only 0.8% of the values near these limits; another 13.4% of the satellite pixels were rejected because multivalued-solution conditions were encountered (cf. Nakajima and King 1990).

a. Continental–maritime contrast

One consideration left out of the above discussion is that the mean droplet radius attained in a particular cloud depends on the number of droplets initially nucleated. Under similar conditions (same humidity and ascending air velocity), nucleation of more droplets will lead to a smaller mean droplet radius (Squires 1958; Mason 1971; Twomey 1977). Since nucleation of water droplets occurs at much smaller supersaturations by initiating growth of the larger background aerosols, which typically contain at least 10%–20% water by mass (Twomey 1977), the number of cloud droplets is controlled by the number of CCN (cloud condensation nuclei) present in the ascending air (and, to some extent, their composition). Aircraft cloud measurements have suggested a systematic difference of mean cloud droplet radii between continental and maritime clouds: the larger maritime radii are attributed to the much lower aerosol abundances in maritime air (Squires 1958; Mason 1971; Twomey 1977). However, since most maritime aircraft measurements are from areas close to the coast and cloud droplet sizes are also influenced by other meteorological factors that change temporally and spatially, we do not have a complete global survey of the variations of mean cloud droplet radius from in situ measurements.

Figure 8 shows the annual, zonal mean droplet radii obtained from our analysis, separated into land and ocean portions, and Table 5 summarizes global and hemispheric averages. The global mean values are 8.5 μm for land and 11.8 μm for ocean. That the mean effective cloud droplet radius over land is about 3 μm smaller than over ocean is consistent with summaries of the aircraft measurements (e.g., Wallace and Hobbs 1977; Pruppacher and Klett 1978; Rogers and Yau 1989). [Note that the conclusions in these references are all based on observations by Ryan et al. (1972) and Squires (1958).] This difference is also larger than our estimated random errors for individual measurements and slightly larger than estimated bias errors, particularly uncertainties associated with surface reflectance effects. One exception to this general land–ocean difference appears in tropical regions, where continental clouds have droplet radii similar to maritime clouds. Other regional exceptions are discussed below.

Another systematic difference between oceanic and continental aerosols is that their vertical profiles differ (Twomey and Wojciechowski 1969; Dinger et al. 1970; Hoppel et al. 1973). Measurements at various locations [over Arizona, the central Pacific, Alaska, and in con-

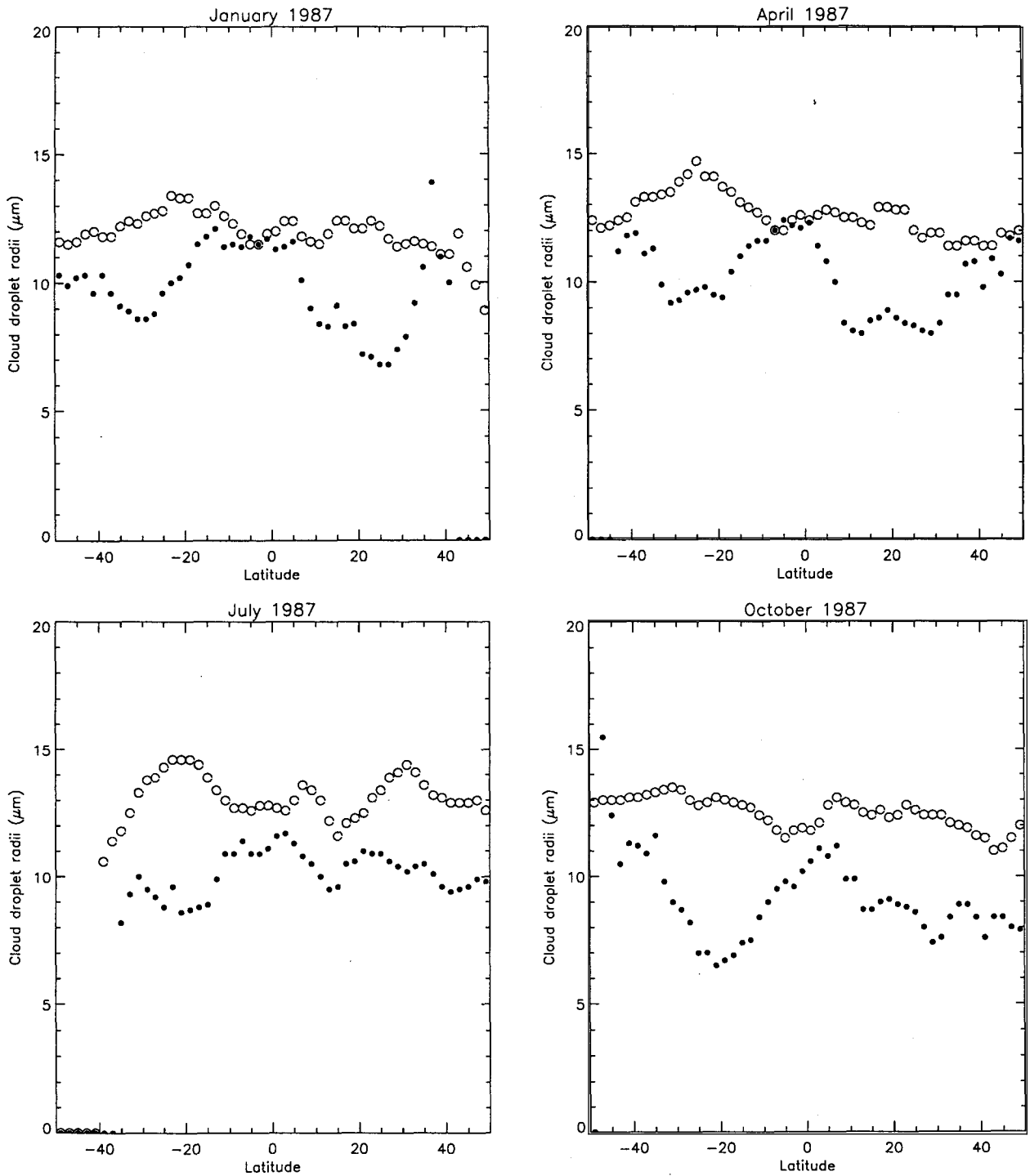

FIG. 8. Monthly, zonal mean effective droplet radii for liquid water clouds for (a) January 1987, (b) April 1987, (c) July 1987, and (d) October 1987 from analysis of *NOAA-9* AVHRR radiances. Open circles are results for clouds over ocean; filled circles are for clouds over land.

vective regions over Florida by Hoppel et al. and over the North Atlantic a few hundred miles southeast of Puerto Rico by Dinger et al. (1970)] show that the aerosol number density decreases with altitude over land by more than a factor of 2 but is relatively constant with altitude over ocean, such that at altitudes > 3 km there is little systematic difference between the oceanic and continental aerosol abundances (Hoppel

TABLE 5. Annual average cloud mean droplet radii r_e (μm), optical thicknesses τ and water paths LWP (g m^{-2}). Results from *NOAA-9* and *NOAA-10* are averaged with equal weights.

		r_e	τ	LWP
Global	Total	11.4	7.0	87.1
	Ocean	11.8	6.9	87.4
	Land	8.5	8.1	85.4
Northern Hemisphere	Total	11.0	6.6	—
	Ocean	11.6	6.4	—
	Land	8.2	7.8	—
Southern Hemisphere	Total	11.7	7.4	—
	Ocean	12.0	7.4	—
	Land	9.0	8.6	—

et al. 1973). This pattern is consistent with the continental surface being the major source of CCN by direct injection processes, but the surface being only one of at least two sources over ocean. Sea salt nuclei from the sea surface are a minority of the total CCN (Twomey 1977); formation of CCN within the atmosphere by sulfur compound gas-to-particle conversion processes provides a source at higher altitudes.

Such a difference in the CCN abundance profiles explains an increase in the land–ocean contrast of cloud droplet radii in our results as cloud-top height decreases. Figure 9 shows the annual zonal mean droplet radii over ocean and land for two different cloud-top temperature/pressure criteria: the first criterion is the standard $T_C > 273$ K (about equivalent to $P_C > 600$ mb), which includes all water clouds, and the second isolates lower-level clouds with $P_C > 750$ mb. The mean droplet radii are the same for both cloud categories over ocean, but the lower clouds over land show smaller radii. Note that the altitude dependence is stronger in the summer hemisphere. This difference may also be due, in part, to a larger height difference in summer between the 273 K temperature level and the 750-mb level.

b. Hemispheric contrast

The difference in the contribution of anthropogenic-sources of aerosols between the Northern and Southern Hemispheres may cause another systematic difference of average cloud particle radii (e.g., Schwartz 1988; Slingo 1988; Wigley 1991; Charlson et al. 1992), although Schwartz's (1988) analysis showed no indication of a significant cloud albedo enhancement (assumed to be an indirect indication of particle size differences) in the Northern Hemisphere compared with the Southern Hemisphere. Figure 10 shows our annual average, zonal mean cloud droplet radii over land and ocean for both hemispheres: for 1987 and 1988, at least, the mean cloud droplet radii in the Northern Hemisphere are smaller than in the Southern Hemisphere

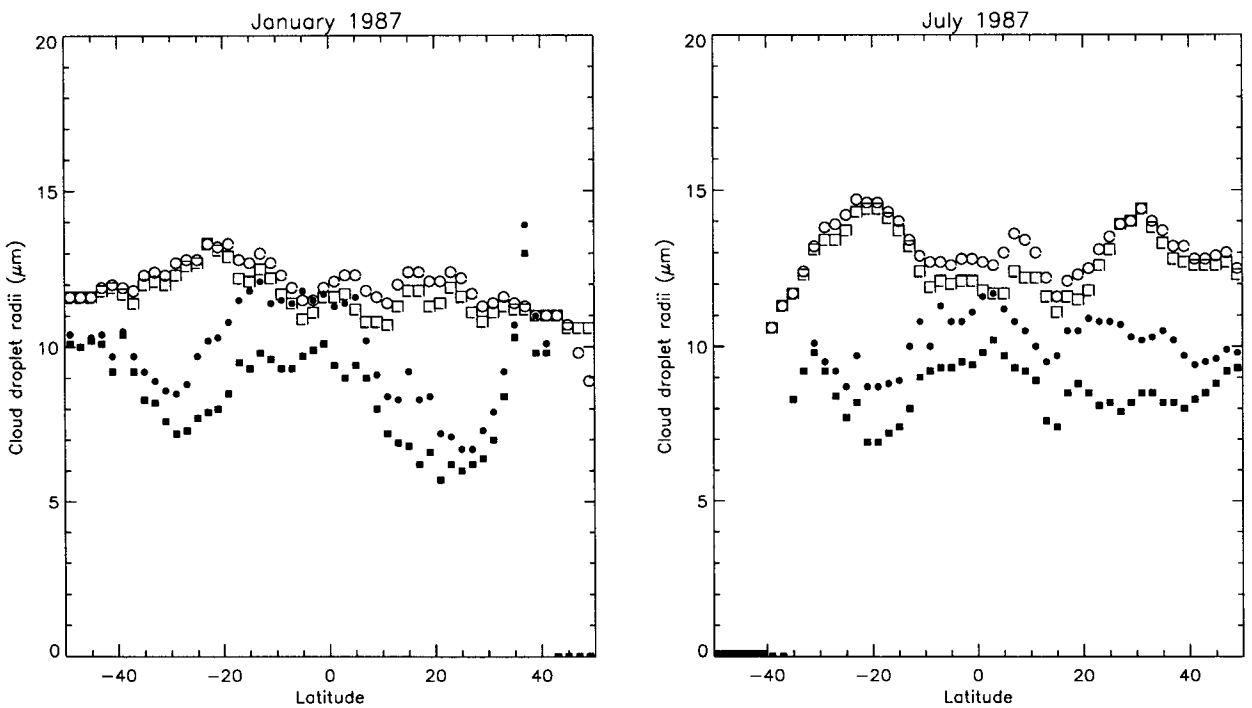

FIG. 9. Monthly, zonal mean effective droplet radii for liquid water clouds for (a) January 1987 and (b) July 1987 from analysis of *NOAA-9* AVHRR radiances with two different cloud-top pressure thresholds: $P_C > 600$ mb (circles) and $P_C > 750$ mb (squares). Open symbols represent results for clouds over oceans, and filled symbols are for clouds over land.

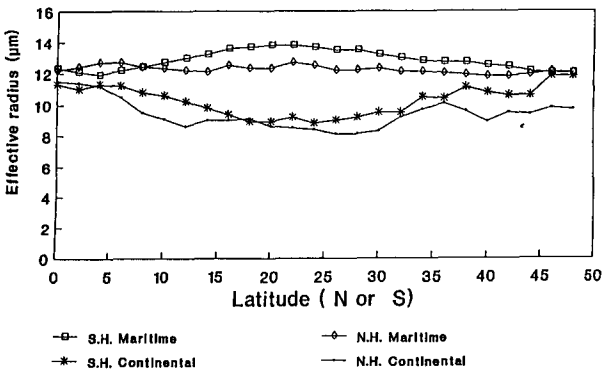

FIG. 10. Annual (4-month average), zonal mean water cloud droplet effective radii for 1987 from analysis of *NOAA-9* AVHRR radiances. Open symbols represent clouds over ocean; filled symbols represent clouds over land. Northern Hemisphere results are shown by diamonds and dots; Southern Hemisphere results are shown as squares and stars.

by about 0.7 μm (Table 5) with the maritime difference somewhat smaller than the continental difference.[1] If we assume equal liquid water contents for clouds in both hemispheres, then the ratio of CCN number densities between hemispheres, needed to explain the droplet radius difference, is 1.10–1.50, less than the 2–3 estimated by Schwartz (1988). That Schwartz does not find a difference in mean cloud albedos, even though the mean droplet radii in the two hemispheres differ, may be explained by the higher mean optical thicknesses of Southern Hemisphere clouds compared with Northern Hemisphere clouds (Table 5). That both the cloud optical thickness and droplet radii differ between hemispheres argues for caution in assuming that a change in CCN abundance will necessarily result in a change in cloud albedo, but our direct determination of droplet sizes suggests that an aerosol effect is present.

c. *Regional variations*

Besides the general contrast in continental–maritime cloud particle radii, there are other significant regional features (Fig. 11). The effect of persistent trade winds can be seen off the subtropical west coasts of Africa, America, and Australia, where smaller than average droplet radii appear, consistent with the winds carrying continental air with higher CCN number densities into adjacent ocean areas (cf., Prospero et al. 1983; Minnis et al. 1992). Similarly, smaller droplet radii appear off the midlatitude east coasts of North America and Asia in winter, these can be explained by aerosol transport by way of stronger westerlies in that season.

There are significant subtropical minima of cloud droplet radii over land (Figs. 8 and 11), which may result from lower relative humidities in the descending motion of the Hadley circulation and higher CCN number densities in the desert environments (Africa and Australia). Notably in summer the clouds forming in the near-coastal parts of the deserts have larger droplet radii than inland clouds, but smaller droplet radii than clouds over more remote oceans, suggesting a reduction of desert aerosol concentrations in mixing with maritime air near the coast. The very small droplet radii obtained in interior desert regions (Fig. 11) may also be, in part, a direct detection of dust (Han 1992).

Much larger droplet radii are found in low-level clouds in the tropical convective regions over the Amazon Basin and Indonesia. During the wet season, frequent precipitation may reduce the CCN number density and make cloud droplet radii larger (Browell et al. 1990). Strong ventilation of the boundary layer by convection, associated with stronger, low-level, horizontal transports of water vapor from nearby oceans, may suppress aerosol concentrations over these land areas and explain a general reduction of the maritime–continental cloud droplet radius contrast (Fig. 8). We may also be detecting the expected average increase of droplet radii when more massive precipitating clouds are more frequent. Some of the larger values may also be associated with cirrus contamination. During the dry season over Amazonia, some of the larger droplet radii might be caused by including optically thin smoke hazes.

The several small regions around high mountains in midlatitudes that exhibit larger cloud droplet radii may be caused by cirrus contamination, which is also suggested by the unusually low numbers of pixels analyzed.

d. *Seasonal variations*

Over India and Southeast Asia the monsoon precipitation cycle shows a landward progression from January through July and a regression from July through January, as shown in the ISCCP results by an increase of average cloud optical thickness and cloud-top height from January through July and a decrease from July through January. In our results, the mean cloud droplet radii also changes from smaller values in the dry season (January) to larger values in the wet season (July) (Fig. 11). Similarly in South America, where January–April is the wet season, an area with larger cloud droplet radii ($r_e > 10$ μm) covers most of South America, except along the west coast where precipitation is also much less. In the dry season (July–October) smaller droplet radii ($r_e < 10$ μm) spread over most of South America (Fig. 11). The same behavior occurs over equatorial Africa. This behavior is consistent with an association of more frequent rainfall from low clouds

[1] For the bias errors to explain this hemispheric difference in average r_e, there would have to be a systematic hemispheric difference of cloud element size distribution (partial pixel cover effect) or of cirrus cloud amount, optical thickness, or both. We cannot rule out such a systematic difference, but note that the consistency of the hemispheric difference of r_e with other indicators of aerosol effects provides a sufficient explanation.

with larger droplet sizes (Albrecht 1989) and reduced CCN abundances because of precipitation scavenging (e.g., Leaitch et al. 1983).

Over North America, maximum precipitation occurs near the west coast in January and near the east coast in July. The seasonal changes in cloud droplet radii are consistent, being larger near the west coast in January and larger near the east coast in July.

In North Africa (Sahara desert) and Saudi Arabia, where precipitation amount is less than 25 mm/season, the mean cloud droplet radii are 2–4 μm all year round (Fig. 11). This result may also be explained, in part, by inclusion of dust clouds (0.1–1 μm of radius but their apparent size might be larger because of larger absorption). In Australia, which has more precipitation than North Africa and Saudi Arabia and larger seasonal variations (January is the wet season), droplet radii are noticeably larger in January. A similar seasonal variation occurs in South Africa, where January is the wet season (larger droplet radii) and July is the dry season (smaller droplet radii).

Table 6 summarizes the seasonal variations of cloud droplet radii and optical thicknesses. Over land, cloud particle radii are generally larger and optical thicknesses are smaller in summer, whereas both cloud particle radii and optical thicknesses are larger in summer over oceans. The magnitude of the seasonal variations is larger over land.

e. *Morning–afternoon contrast*

NOAA-9 is in an "afternoon" sun-synchronous polar orbit (equatorial crossings at local times of 1400–1600 and 0200–0400) and *NOAA-10* is in a "morning" orbit (crossings at local times 0730–0830 and 1930–2030). Analysis of radiances from these two satellites provide "morning" (*NOAA-10*) and "afternoon" (*NOAA-9*) observations of effective droplet radii of liquid water clouds.

Figure 12 shows the geographic distribution of the differences between monthly mean droplet radii from *NOAA-10* and *NOAA-9* ("afternoon" minus "morning") and Table 7 provides a summary. Because of limitations on the smallest solar zenith angles at which retrievals can be made, results are only available for *NOAA-10* from latitudes north of 20°S in July and south of 30°N in January; results are shown in Fig. 12 for spring and autumn, averaged over 1987 and 1988, to maximize the latitude range covered. Also, since our retrieval may be biased by broken cloud effects at the most extreme solar zenith angles, diurnal variations at high winter latitudes may be spurious. At lower latitudes, most clouds have larger droplet radii in the afternoon than in the morning, except over deserts, where cloud droplet radii are larger in the morning. The magnitude of the changes is somewhat larger in the areas of more frequent deep convection, so these results may be affected by diurnally varying cirrus contamination.

Figure 13 (Table 7) shows the morning–afternoon differences of cloud optical thickness for April and October (averaged over 1987 and 1988). Together, Figs. 12 and 13 show that most areas with large morning to afternoon droplet radius increases also exhibit morning to afternoon cloud optical thickness decreases. This correspondence is most evident in areas dominated by marine stratus clouds. In contrast, the more arid land areas show increasing morning to afternoon cloud optical thicknesses, consistent with increased convective activity in summer afternoons.

The general diurnal variation of r_e that we find for marine stratus clouds appears to contradict observations from FIRE (Minnis et al. 1992), even though our diurnal variations of cloud amount and optical thickness agree (Rossow and Schiffer 1991). When we isolate our results for the FIRE experiment site, however, we find a similar variation of r_e consistent in sign with the results of Minnis et al. (1992). Our results show decreases in r_e and τ of about 2 μm and 3, from 0730 to 1515 local time; the corresponding values from Minnis et al. (1992) show decreases of about 5 μm and 5, respectively. Thus, we conclude that the near-coastal marine stratus regime observed by FIRE may not be typical of marine stratus farther from land.

Albrecht (1989) studied drizzle formation in shallow (boundary layer) marine clouds and noted, particularly, the difference in the width of the droplet size spectra between maritime and continental boundary-layer clouds. He proposed that the broader droplet size distribution in shallow maritime clouds enhances precipitation formation in the form of drizzle, implying a morning to afternoon increase in droplet radii accompanied by a morning to afternoon decrease of cloud optical thickness. No information about the diurnal variation of drizzle is available, however. Other studies of marine stratus formation have concentrated on changes in the coupling of the surface to the planetary boundary layer, which imply changes in turbulent mixing that might cause similar morning to afternoon evolution in cloud properties (cf. Nicholls 1984).

At higher latitudes, the morning to afternoon contrast in droplet radii is very small over ocean areas. Midlatitude continental clouds exhibit two different regimes. The more arid regions in western North America, central Asia, southern Australia, and Argentina all show larger cloud droplet radii in the morning similar to lower-latitude deserts. This behavior is consistent with observations of continental cumulus in similar areas (e.g., Jensen et al. 1985). In contrast, the moister areas in eastern North America, Europe, and eastern Asia all show slightly larger droplet radii in the afternoon.

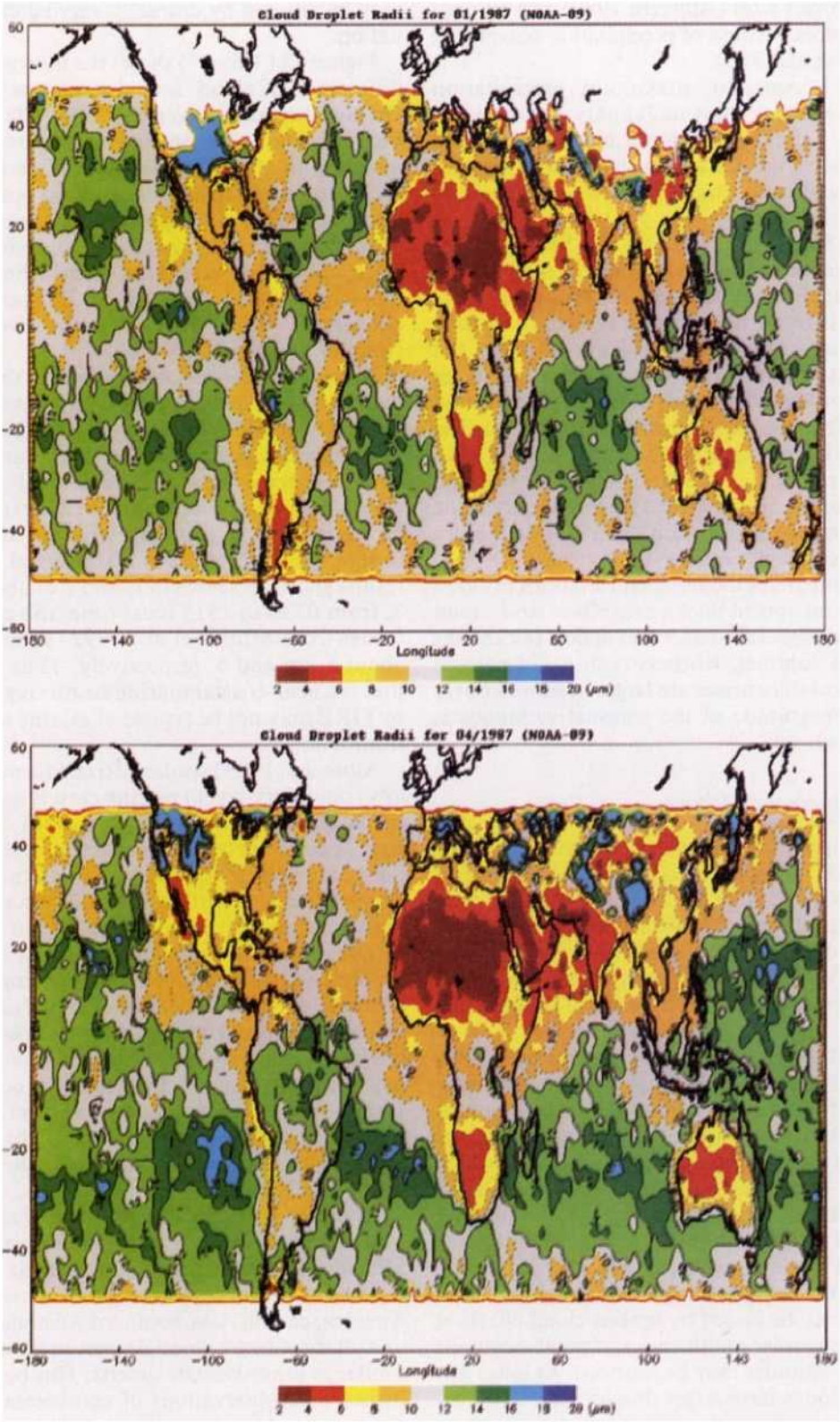

FIG. 11. Geographic distribution of water cloud effective radii (in microns) averaged over analysis results from *NOAA-9* AVHRR radiances and over corresponding months in 1987 for (a) winter (January), (b) spring (April), (c) summer (July), and (d) autumn (October).

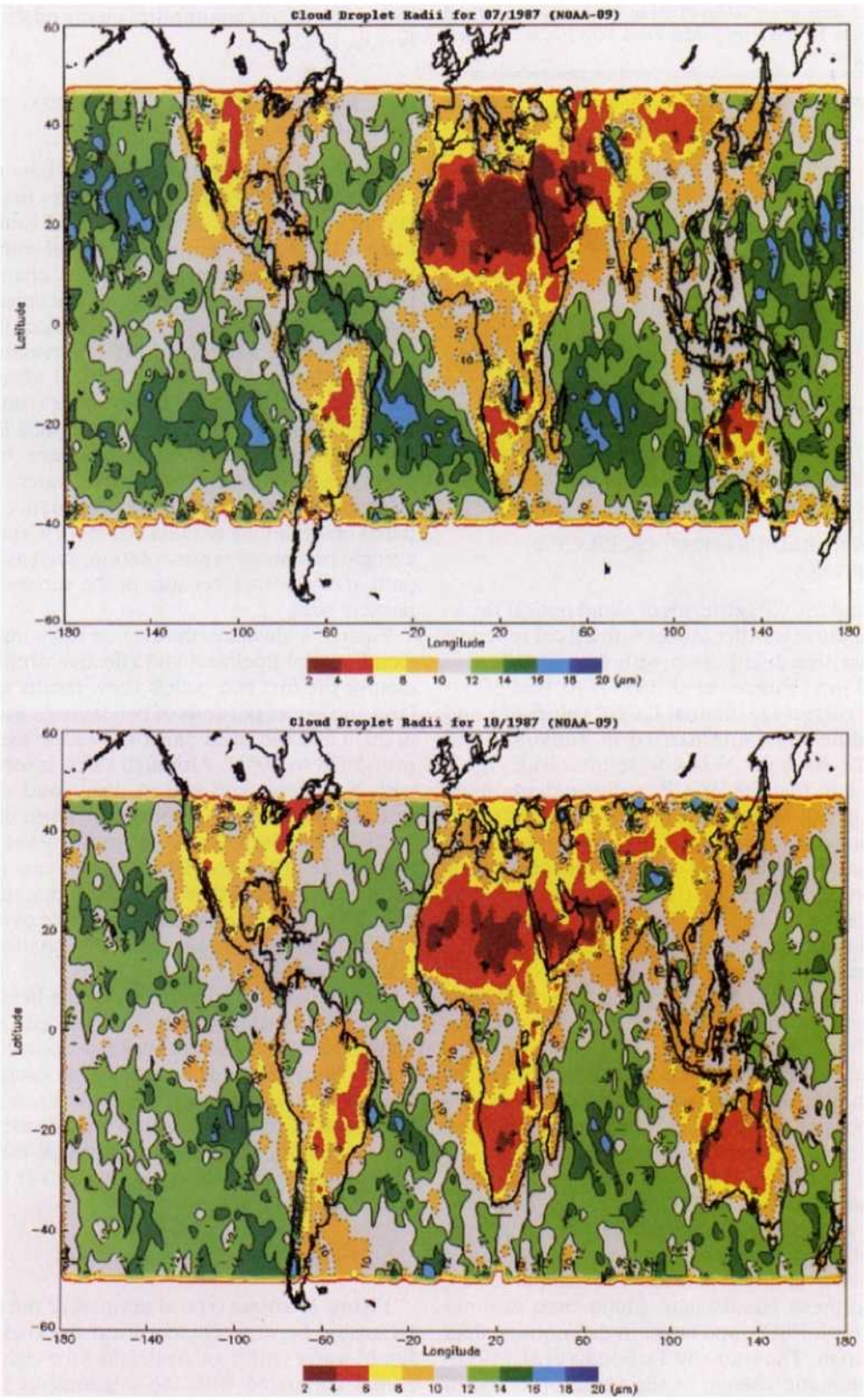

FIG. 11. (*Continued*)

TABLE 6. Seasonal mean values of cloud droplet radii (μm) and optical thicknesses. Results from *NOAA-9* and *NOAA-10* are averaged with equal weights.

	Winter	Spring	Summer	Autumn
		Land		
NH r_e	7.6	7.8	9.0	7.8
NH τ	9.5	6.7	7.7	9.0
SH r_e	9.0	8.1	9.3	9.4
SH τ	10.8	8.0	8.0	8.8
		Ocean		
NH r_e	10.2	11.6	12.2	11.7
NH τ	6.4	5.8	6.8	6.4
SH r_e	11.6	12.6	11.6	11.4
SH τ	7.4	7.4	7.5	6.4

f. Relationships among cloud droplet radius, optical thickness, and water path

1) DROPLET RADIUS EFFECT ON ISCCP τ RETRIEVALS

The original ISCCP retrievals of cloud optical thickness use a radiative transfer model with a fixed spherical water droplet size distribution with a mean effective radius of 10 μm (Rossow et al. 1991). As part of our analysis, we correct the original ISCCP values of τ and record the difference, summarized in Table 8. Averaging *NOAA-10* and *NOAA-9* results with equal weights, we find that the ISCCP results underestimate the annual, global mean cloud optical thickness of liquid water clouds by about 1.5%. For ocean clouds the underestimate is about 1.5%–2% and for land clouds the ISCCP results overestimate optical thicknesses by about 1%–2% (cf. Table 5). The general decrease of optical thicknesses in low-latitude clouds over the day is overestimated by about 1% (cf., Table 7). The standard deviation of cloud droplet radii, ± 5.6 μm, implies a random error in the ISCCP optical thickness values of about $\pm 7\%$.

Using our optical thickness values corrected for variations in droplet radius, we checked some systematic differences in cloud optical thicknesses found in the ISCCP results (Rossow and Schiffer 1991; Tselioudis et al. 1992), as well as in a previous analysis (Rossow and Lacis 1990). Tables 5, 6, and 7 confirm these earlier results: cloud optical thicknesses are larger at higher latitudes than at lower latitudes and larger over land than over ocean (Rossow and Schiffer 1991), larger in Northern Hemisphere winter than summer (Tselioudis et al. 1992), and larger in the morning than in the afternoon. The study by Tselioudis et al. (1992) found a systematic change in the variation of cloud optical thicknesses between cold and warm clouds, but their findings are based on the assumption that the cloud particle radii are constant. A reanalysis of the optical thickness variations using our results indicates little effect of this assumption on the relationship (Tselioudis 1992).

2) RELATIONSHIP BETWEEN OPTICAL THICKNESS AND DROPLET RADIUS

There is some controversy about how much cloud microphysics information is necessary to model cloud effects on radiation. Somerville and Remer (1984), using a 1D radiative-convective model with fixed cloud particle sizes and optical thickness changes proportional to water content changes, concluded that cloud optical thickness feedback is significantly negative. Based on a summary of regional observations, Stephens (1978) suggested that cloud optical effects could be modeled in terms of the cloud water content without other information on cloud microphysics. Platt (1989), however, argued that cloud particle size changes could offset the radiative effects of cloud water content variations. Moreover, Curry and Herman (1985) compared observations to radiative models and found that a single-parameter representation, such as liquid water path, did not work because of the variability of cloud particle sizes.

Figure 14 illustrates the average relationship between cloud optical thickness and effective droplet radius of clouds: the first two panels show results split into the land and ocean portions of two latitude zones (divided at 30°) and the third panel shows the average results over 50°S to 50°N. Although there is some variation with geography and season, the cloud droplet radii generally increase with optical thickness up to about $\tau = 20$–30 and decrease for optically thicker clouds. The magnitude of the droplet radius increase is somewhat larger in the tropics than in midlatitudes; tropical ocean clouds show the largest change, a little over 5 μm, and midlatitude land clouds show the smallest change, a little under 2 μm.

The only notable exception to the behavior shown in Fig. 14 is in some regions where droplet radii sharply increase to $r_e > 14$ μm at very low optical thicknesses, $\tau < 2$. Some of these cases may be caused by cirrus contamination; however, some locations (e.g., off the west coast of north Africa and off the east coast of the United States in summer) suggest that these "clouds" are not water clouds but rather unusually thick aerosol hazes (see discussion in section 4d).

3) CLOUD LIQUID WATER PATH

Figure 15 shows typical samples of the observed relationship between cloud optical thickness and cloud liquid water path (see Appendix) for eight latitudinal zones, compared with the relationship suggested by Stephens (1978) and the range of relationships observed by Curry and Herman (1985). We find that our results agree with Stephens' suggestion for the midlatitude continental and subtropical marine clouds that

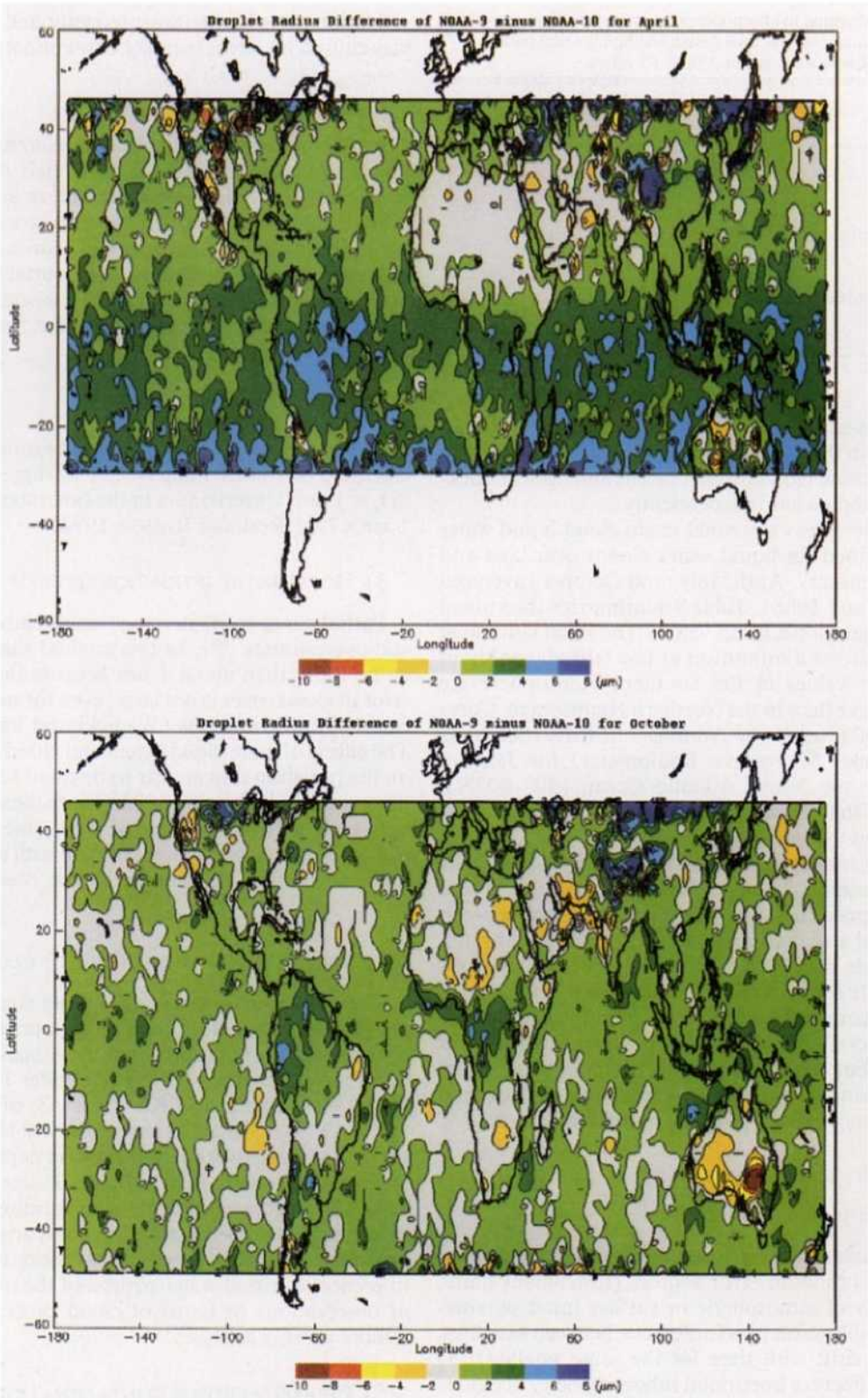

FIG. 12. Geographic distribution of differences between monthly mean effective radius values (in microns) from *NOAA-9* ("afternoon") and from *NOAA-10* ("morning") averaged over (a) spring (April 1987 and 1988) and (b) autumn (October 1987 and 1988).

TABLE 7. Morning to afternoon contrasts in monthly mean cloud droplet radii (μm), optical thicknesses and liquid water path (g m^{-2}) given as *NOAA-9* values minus *NOAA-10* values.

		Droplet radius	Optical thickness	Water path
Global	Total	0.9	−1.1	11.7
	Ocean	1.0	−1.1	11.3
	Land	0.6	−1.6	15.0
Northern Hemisphere	Total	0.6	−0.8	—
	Ocean	0.8	−0.8	—
	Land	0.3	−1.5	—
Southern Hemisphere	Total	1.1	−1.5	—
	Ocean	1.1	−1.6	—
	Land	1.0	−2.0	—

his datasets sampled. More generally, the relationship varies within the range indicated by Curry and Herman (1985) because cloud droplet radius and optical thickness vary somewhat independently.

Figure 16 shows the zonal mean cloud liquid water paths obtained for liquid water clouds over land and ocean in January, April, July, and October (averaged over 1987 and 1988). Table 9 summarizes the annual and seasonal, global mean values. The small latitudinal variation shows a minimum at low latitudes at about 10°–15°N; values in the Southern Hemisphere are slightly larger than in the Northern Hemisphere. Curry et al. (1990), using the *Nimbus-7* SMMR (Scanning Multichannel Microwave Radiometer) for January 1979 over the North Atlantic Ocean (40°–60°N), concluded that the average liquid water paths for middle and low clouds were 115 and 102 gm^{-2}, respectively. Our results show a value of 113.5 gm^{-2} over the ocean between 40° and 50°N for January 1987. There does not appear to be any simple relationship between continental and maritime values of cloud liquid water path: clouds over land have larger liquid water paths than clouds over ocean in January and April, but almost the same values in July and October. Maritime clouds generally show lower liquid water paths at lower latitudes, but large regional fluctuations suggest that specific changes in regional meteorology may explain more of the variation of cloud liquid water paths.

6. Summary and discussion

a. *Summary of uncertainties*

The sources of error in the retrieved cloud droplet sizes are 1) random error sources (instrument noise, uncertainty of atmospheric or surface input parameters); 2) calibration bias (difference between satellites, sensitivity drift with time for the same satellite); 3) radiative effects of horizontal inhomogeneity of clouds (broken cloudiness, morphology), which may be systematic for boundary-layer clouds; 4) vertical inhomogeneity of clouds (multilayer clouds, droplet size change with altitude within a cloud), which may affect validation using in situ measurements; and 5) a positive bias caused by cirrus/aerosol contamination.

1) RANDOM ERROR

Random errors in individual measurements, attributable to instrument noise in channels 3 and 4, uncertainties of atmospheric temperature and humidity profiles, and the surface temperature, are estimated to be ~10%, based on the narrowest distribution of radii observed. (The atmospheric and surface properties might also introduce bias errors, but assessments of the ISCCP values do not indicate any significant problem in this regard.)

2) CALIBRATION BIAS

Specific checks of possible calibration biases for channel 3 on *NOAA-9* and *NOAA-10* suggest bias errors in $r_e < 1$ μm. Uncertainties in the calibration of channel 1 are <7% (Brest and Rossow 1992).

3) HORIZONTAL INHOMOGENEITY OF CLOUDS

Partial cloud cover in image pixels causes a systematic overestimate of r_e in this method that appears to be no more than about 1 μm because the systematic error in cloud cover is not large, even for marine stratus cloud size distributions (Wielicki and Parker 1992). The effects of finite cloud extent and cloud morphology on the radiation also appear to be small for near-nadir observations (Kobayashi 1993). Since these effects may vary systematically with cloud type, time of day, and season, however, we cannot estimate with any accuracy the contribution they make to the observed variations.

4) VERTICAL INHOMOGENEITY OF CLOUDS

The results are sensitive to droplet sizes in the uppermost one to two units of cloud optical thickness, so that variations of droplet radius with altitude within the cloud (cf. Squires 1958; Noonkester 1984; Durbin 1959; Weickmann and Kampe 1953; Singleton and Smith 1960) suggest that our values will be larger than the true average over the whole cloud depth. Since aircraft measurements of cloud particle sizes are not always identified according to their location within the cloud, care must be exercised in comparisons (cf. Nakajima et al. 1991). This error is more important to inferences of cloud water paths and the interpretation of observations in terms of cloud processes than to remote sensing analyses.

5) CIRRUS/AEROSOL CONTAMINATION

An optically thin, ice cloud layer with large ice crystals overlying a water cloud can appear as a water cloud containing much larger droplets. Aerosol hazes

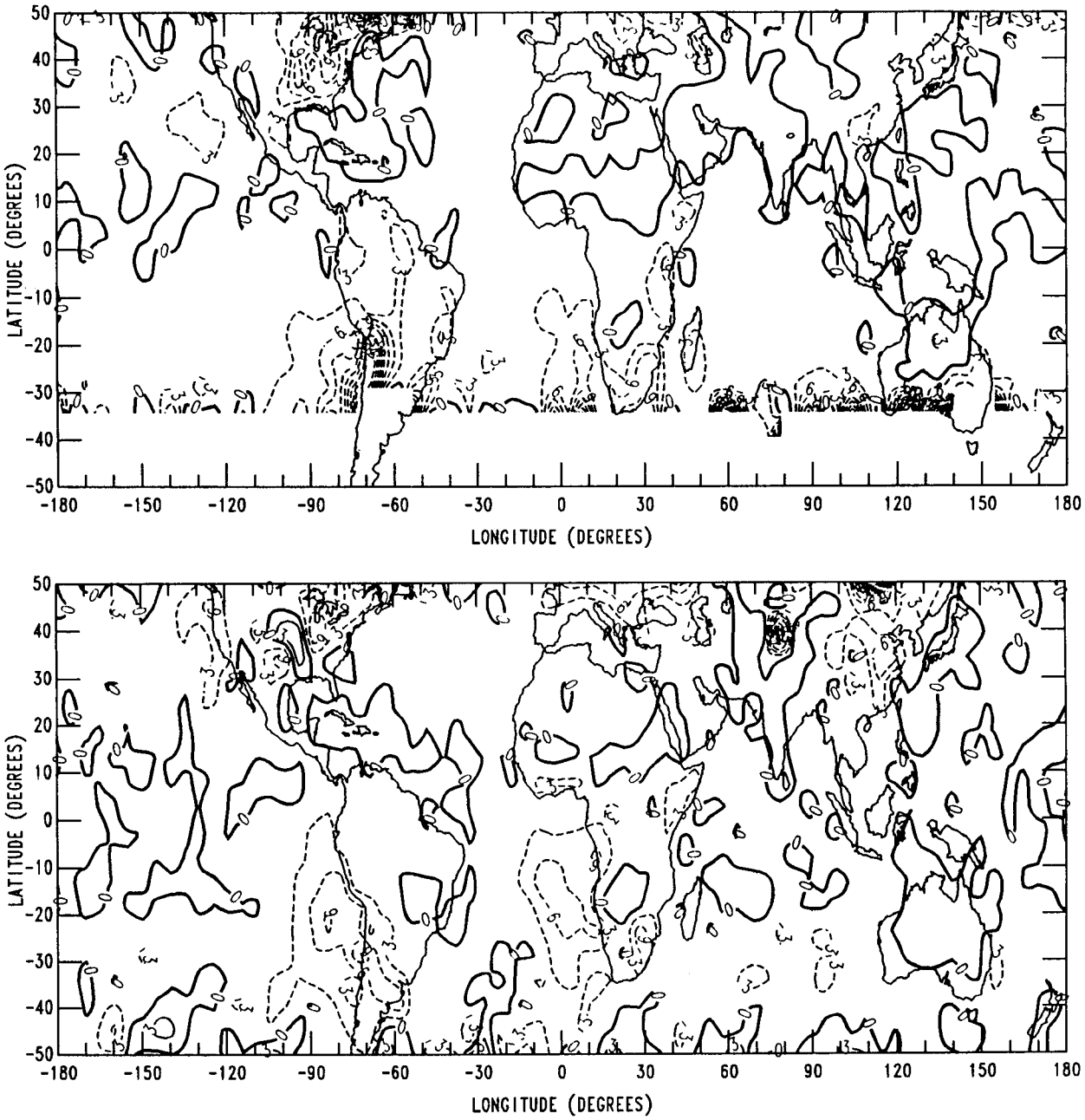

FIG. 13. Geographic distribution of differences between monthly mean cloud optical thickness values from *NOAA-9* ("afternoon") and from *NOAA-10* ("morning") averaged over (a) spring (April 1987 and 1988) and (b) autumn (October 1987 and 1988). Solid contours indicate positive differences and dashed contours indicate negative differences; contour interval is 3.

with very small particles and larger imaginary indices of refraction can appear as optically thin water clouds with large droplet radii. These bias errors appear in our results in specific locations (cirrus effects in the tropics and near mountains and aerosols near deserts or in areas of high pollution), but do not cause any significant bias in the hemispheric and global statistics.

b. Discussion

Channel 3 (3.7-μm wavelength) radiances from AVHRR can be used for retrieving cloud droplet effective radius. The advantages of this wavelength are that the problem of multiple solutions (cf. Nakajima and King 1990) occurs at smaller optical thicknesses and that the effects of surface reflectance are much

TABLE 8. Differences between cloud optical thickness values retrieved assuming a constant droplet radius and a variable droplet radius (ISCCP minus this work). Differences shown are global means from *NOAA-9*. Season names refer to boreal seasons.

	Annual	Winter	Spring	Summer	Autumn
Total	0.13	0.14	0.18	0.07	0.06
Ocean	0.00	0.08	0.12	0.00	0.00
Land	0.60	0.62	0.56	0.53	0.77

smaller (as most surfaces are relatively dark). The disadvantage is that the contribution of thermal emission becomes important for thinner clouds.

Clouds with different composition (dust, soot, water, ice) are usually retrieved as large radius water droplets because of their larger absorption coefficients. In particular, thin cirrus over water clouds may be the largest bias error, but we find that noticeable cirrus contamination appears to be localized.

The annual global mean cloud droplet radius we obtain is 11.4 ± 5.6 μm where over land the average r_e = 8.5 μm and over ocean, r_e = 11.8 μm; all values are area weighted. ISCCP-retrieved cloud optical thicknesses assume a fixed effective particle radius of 10 μm, which produces a low bias of about 1% over oceans and a high bias of about 1%–2% over land with a random error of about 7%.

We find four distinct indicators that variations of the background CCN concentration influence the average cloud droplet radius: land–ocean contrasts in both 1) mean cloud droplet radius and 2) its variation with cloud-top altitude, 3) specific near-coastal variations of cloud droplet radius consistent with wind direction, and 4) systematic hemispheric differences in cloud droplet radius over both land and ocean. Our near-global survey confirms that the average cloud droplet radius in continental clouds is smaller (about 8–9 μm) than in maritime clouds (about 11–12 μm) as had been reported by aircraft measurements with limited spatial coverage. The difference is not as large in the tropics. This difference grows larger for lower-level (P_C > 750 mb) clouds, consistent with observed vertical variations of aerosol concentrations. The transition between land and ocean values of r_e does not occur precisely along coastlines; instead local variations in prevailing wind direction cause penetration of marinelike values inland or continentlike values out to sea.

Comparison of hemispheric mean values of cloud droplet radius shows an interhemispheric difference that is qualitatively consistent with, but smaller than predicted from, observed differences in CCN concentrations between the two hemispheres. Schwartz (1988) searched for the "indirect aerosol effect on clouds" by comparing cloud albedos between the two hemispheres, but he found no significant differences. Slingo (1988) pointed out that cloud albedos might depend on other cloud properties, such as liquid water content. Our direct comparison of mean cloud droplet radii between hemispheres shows a systematic difference in r_e, but also shows a systematic difference in the cloud optical thicknesses approximately sufficient to explain why Schwartz could not find hemispheric differences in cloud albedo. After correcting ISCCP optical thickness values for variations in cloud droplet radius, we also confirm that continental clouds still have larger optical thickness values than maritime clouds (Rossow and Lacis 1990; Rossow and Schiffer 1991). All of these results support the existence of an aerosol effect on cloud droplet radii, but they also support Slingo's reservation that other factors may play an equally important role in determining cloud albedos.

Clouds in the Northern Hemisphere over both land and ocean show a significant seasonal variation of mean droplet radii while those in the Southern Hemisphere do not. If seasonal variations in the CCN number density and cloud dynamics were the same for both hemispheres, then variations in liquid water content, I, with temperature would control cloud droplet radii. If I increases with increasing temperature (Somerville and Remer 1984; Betts and Harshvardhan 1987), then r_e should be larger in the summer hemisphere and smaller in the winter hemisphere. We observe larger r_e in summer, but the magnitude of the seasonal cycle is not the same for both hemispheres. After correcting the ISCCP optical thickness values for variation in cloud droplet radii, we confirm the previous finding (Tselioudis et al. 1992) that warmer clouds generally have lower optical thicknesses; we also find that the seasonal variations of optical thickness differ between the two hemispheres. Thus, although r_e follows the predicted change in I, τ does not. Taken together, these differences in behavior may be explained by different seasonal variations in atmospheric circulation. The variations of cloud properties with meteorological conditions deserve much more detailed scrutiny to confirm their dependence on temperature, CCN concentration, and atmospheric motions.

For most maritime clouds and some continental clouds, droplet radii are larger and optical thicknesses smaller in the afternoon than in the morning: the largest variations in r_e occur at lower latitudes, where the average magnitude of the change is 3–4 μm, while at higher latitudes the changes are only about 1 μm and may not be significant. Some continental clouds, particularly over the more arid locations, have smaller droplet radii and larger optical thicknesses in the afternoon than in the morning.

Maritime water clouds exhibiting significant diurnal variations are formed in the boundary layer, predominantly in the early morning. Nicholls (1984), based on aircraft observations of turbulence mixing, radiative fluxes, and the microphysics in stratocumulus clouds over the North Sea, suggested that the absorption of sunlight and entrainment of dry air from above cloud

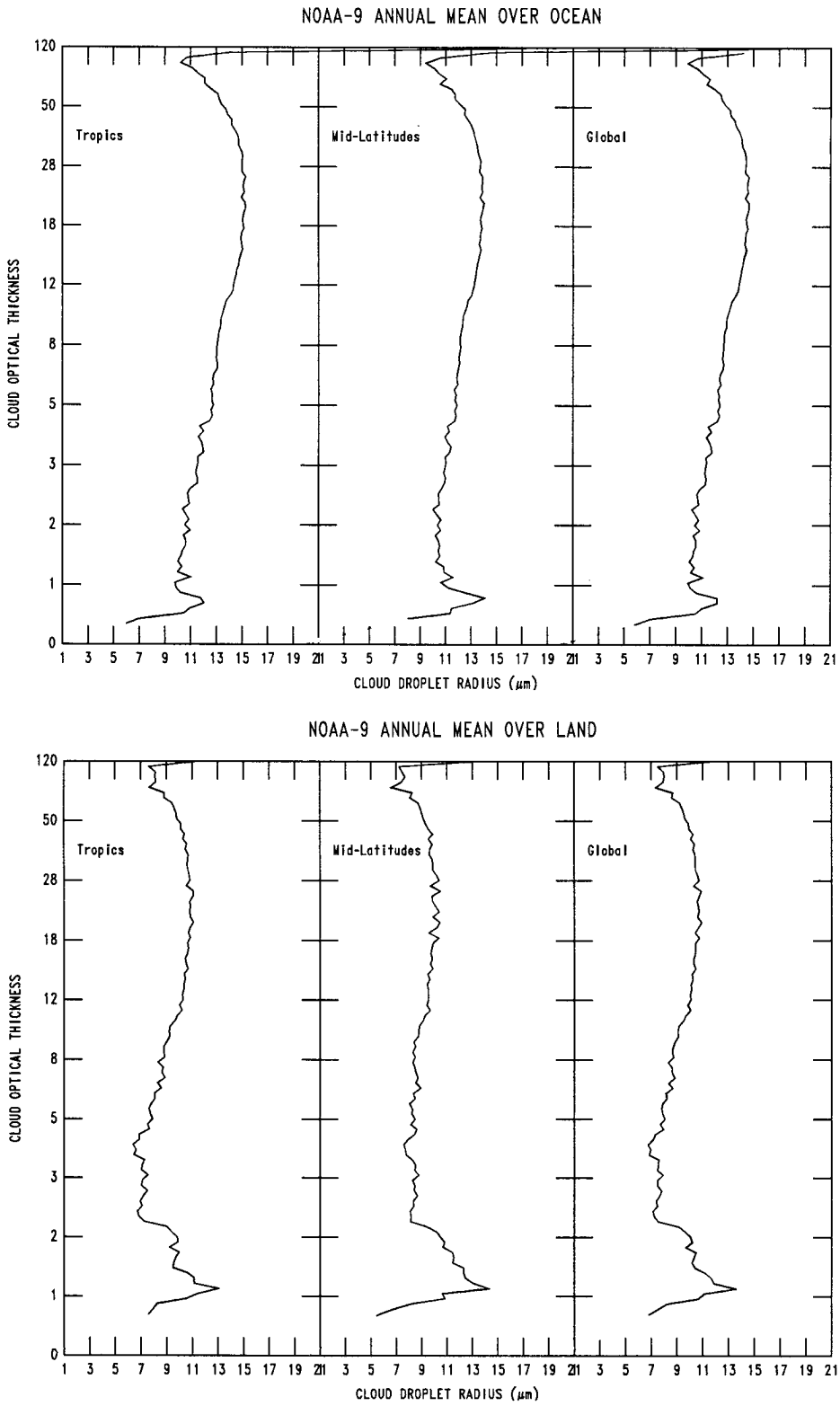

FIG. 14. Annual average cloud droplet effective radius in each interval of cloud optical thickness from analysis of *NOAA-9* AVHRR radiances in the tropics (latitude < 30°), midlatitudes (latitude between 30° and 50°), and over the whole globe (latitude < 50°) for (a) clouds over ocean and (b) clouds over land.

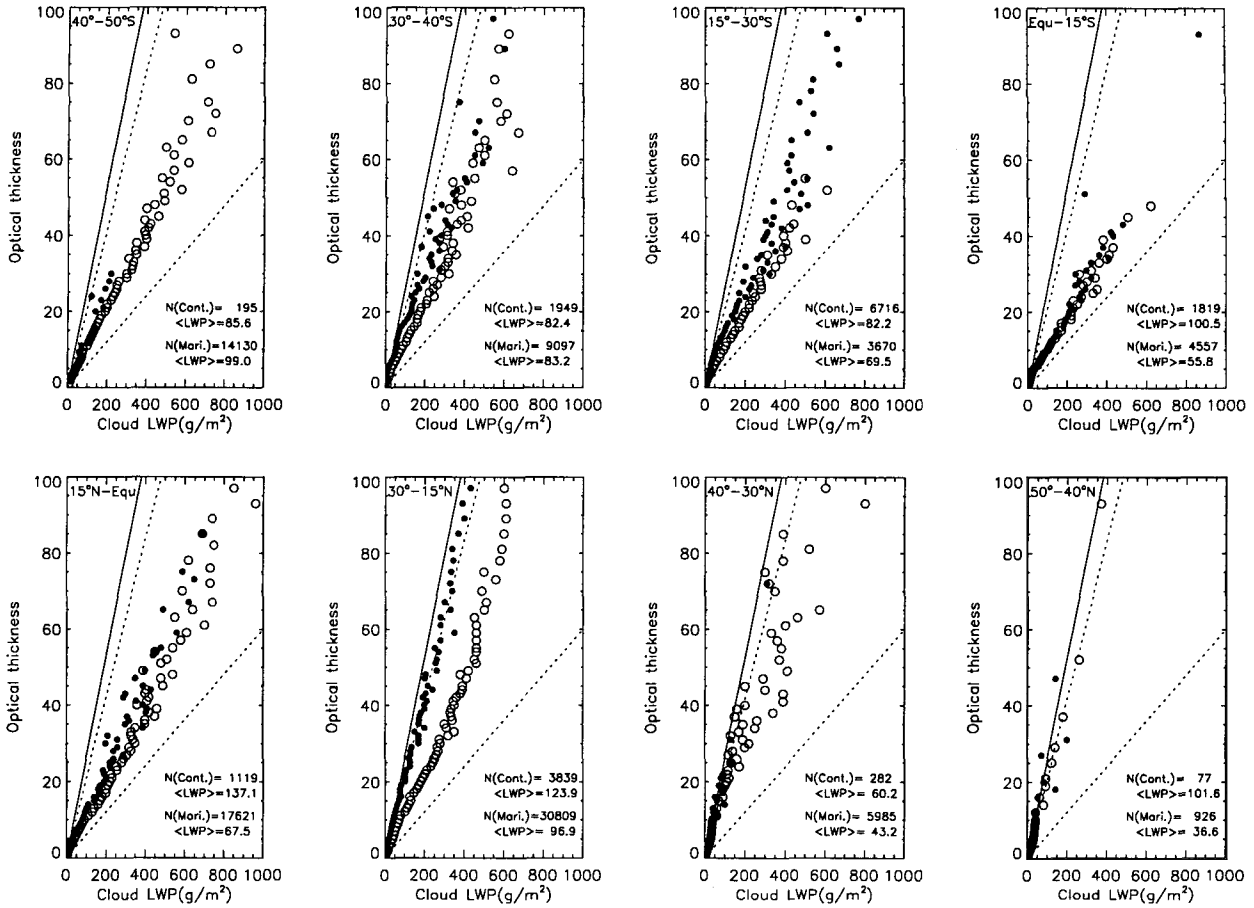

FIG. 15. Monthly (January 1987) mean cloud optical thickness in each interval of cloud liquid water path derived from effective radius and optical thickness retrievals from *NOAA-9* AVHRR radiances for various latitude zones. Solid line shows relationship proposed by Stephens (1978), and dashed lines show range of observations reported by Curry and Herman (1985). Number of points, N, and average liquid water path, LWP, values are shown. Filled circles are for clouds over land; open circles are for clouds over ocean.

top causes the droplet number density to decrease dramatically and the drop sizes to increase over the course of the day. Telford and Wagner (1981), from their observations of convective maritime stratus cloud, suggested that the entrainment of dry overlying air dilutes the liquid water content by evaporation, sometimes by a factor of 10. Consequent evaporation in entrained dry air initially reduces the droplet concentration without reducing their size, but as these parcels mix lower into the cloud, larger droplets are produced, sometimes exceeding 30 μm in diameter. Albrecht (1989), on the other hand, suggested that the drizzle process in shallow marine clouds produced droplet size spectrum broadening during the day and argued that this difference allowed shallow maritime clouds to form precipitation more easily than continental clouds, consistent with the findings of Jensen et al. (1985). The development of drizzle over the course of the day could explain both an increase of droplet radii and a decrease of optical thickness (the latter because of decreasing cloud vertical extent).

Boundary-layer clouds over continents form mostly in the afternoon (Stull 1988). From a case study of nonprecipitating continental cumulus clouds in eastern Montana, Jensen et al. (1985) determined from a microphysical model that even when drier air is entrained into the clouds, the droplet spectra can remain narrow because the characteristic time for droplet evaporation is much larger than that for eddy diffusion at normal turbulence levels in continental cumuli. Thus, in land areas with sufficient moisture supply, solar heating may increase the turbulent supply of water vapor and cause growth of cloud droplet radii in the afternoon. We see increasing r_e values in locations of greater moisture. In more arid locations, the decrease of droplet radii we observe during daytime may be caused by an enhanced turbulent flux of surface dust over the daytime. The associated increase of cloud optical thicknesses over deserts may be due to increasing turbulence and cloud vertical extents in the afternoon.

We find that cloud droplet radii generally increase with optical thickness for optically thinner clouds (τ

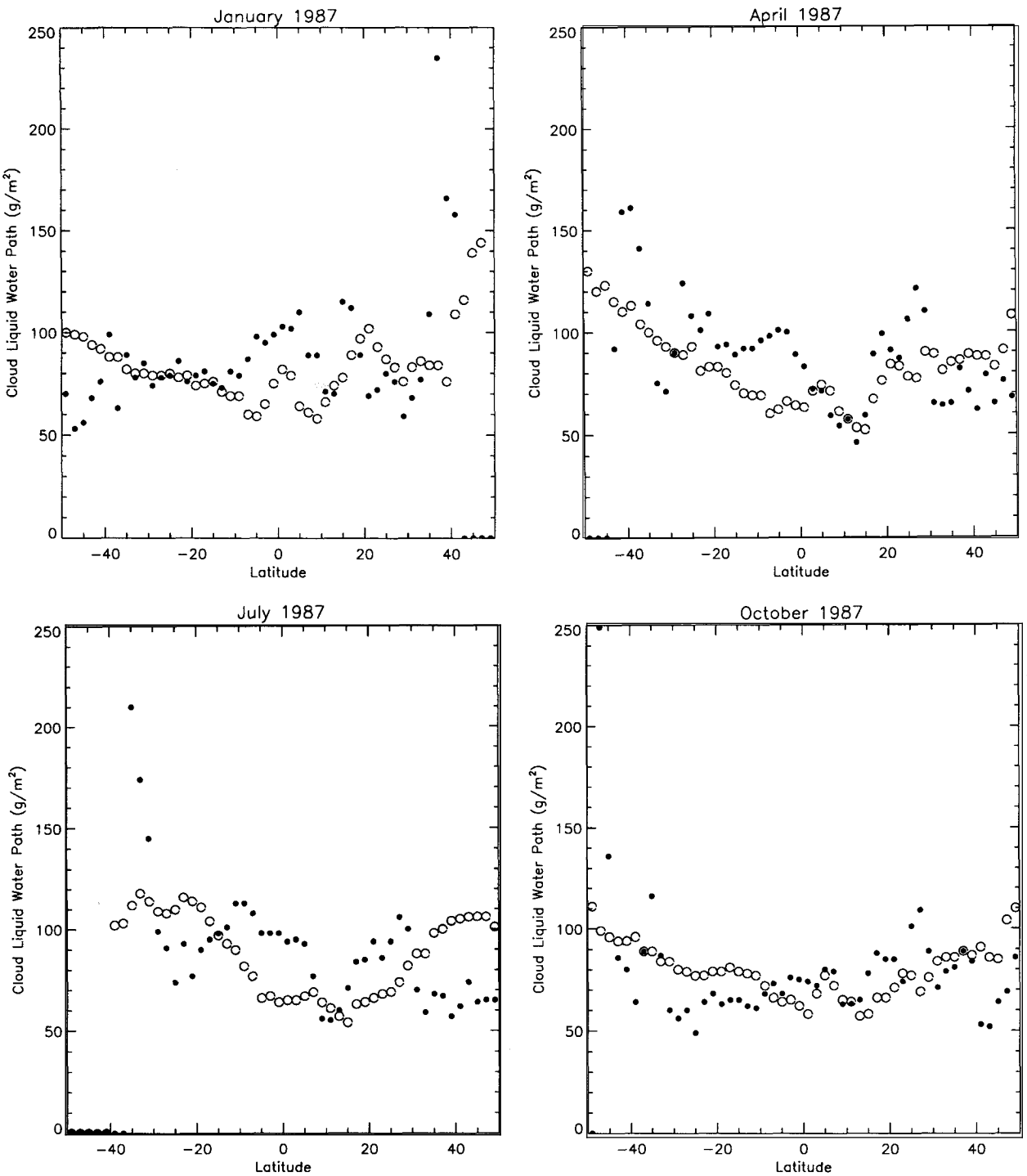

FIG. 16. Monthly, zonal mean cloud liquid water paths obtained from retrievals of cloud droplet effective radius and optical thickness from *NOAA-9* AVHRR radiances for (a) January 1987, (b) April 1987, (c) July 1987, and (d) October 1987. Open circles are for clouds over ocean; filled circles are for clouds over land.

< 20–30) and decrease for optically thicker clouds, but that this relationship varies with location and season. This transition can be explained by a general predominance of condensation growth control of average droplet radius in thinner (lower water content?) clouds giving way to a predominance of collision growth control of average droplet radius in thicker (higher water content?) clouds. However,

TABLE 9. Annual and seasonal mean values of cloud water path (gm^{-2}) over ocean and land from 1987 and 1988. Annual mean is represented by the average of 4 months; *NOAA-9* and *NOAA-10* results are averaged with equal weights.

	Annual	January	April	July	October
Ocean	87.4	89.1	80.2	89.6	90.8
Land	85.4	91.3	77.0	86.3	87.0

some clouds, particularly marine stratus, exhibit diurnal variations where r_e increases while τ decreases. In the FIRE case, optical thickness decreased, in part, because cloud layer thickness decreased (Minnis et al. 1992). We also find that cloud liquid water path is not uniquely related to cloud albedo, because significant and somewhat independent variations of cloud optical thickness and droplet radii are observed. For all these reasons, the specification of both average cloud droplet effective radius and cloud water content (or optical thickness and vertical extent) is necessary to model the radiative effects of clouds in climate GCMs.

Acknowledgments. We thank the following people for their comments and advice: Barbara Carlson, Anthony Del Genio, Inez Fung, and James Hansen. We also thank Albert Arking for the inspiration. Special thanks to Alison Walker for assistance with the ISCCP datasets, production of final summary statistics, and processing of the larger dataset that forms the basis for this study. We appreciate very valuable comments from three anonymous reviewers, which helped us shape and improve this paper. The basic model used for this analysis was developed by Ina Vulis, but her untimely death in April 1988 prevented her participation in the completion of this study. This research was supported by the NASA Climate Program managed by Dr. James Dodge; the ISCCP international manager is Dr. Robert A. Schiffer. The ISCCP is part of the World Climate Research Program supported by the efforts of several nations. One of us (QH) acknowledges the partial support under NASA Contract numbers NAS1-19077 and NAG-1-542.

APPENDIX

Basic Formula for Cloud Properties

a. Cloud optical thickness and liquid water path

Cloud optical thickness is given by

$$\tau(\lambda) = \int_0^h \int_0^\infty \sigma_{\text{ext}}(\lambda, r) n(r) dr dh', \quad \text{(A.1)}$$

where $\sigma_{\text{ext}}(\lambda, r)$ is the extinction cross section of a spherical water droplet of radius r at wavelength λ; $n(r)dr$ is the number of particles per unit volume with radius between r and $r + dr$, and h the cloud layer thickness. We substitute the normalized extinction cross section (efficiency for extinction)

$$Q_{\text{ext}}(\lambda, r) = \frac{\sigma_{\text{ext}}(\lambda, r)}{\pi r^2}; \quad \text{(A.2)}$$

then

$$\tau(\lambda) = \pi \int_0^h \int_0^\infty Q_{\text{ext}} r^2 n(r) dr dh'. \quad \text{(A.3)}$$

The normalized extinction cross section $Q_{\text{ext}}(\lambda, r)$ is a complicated function of r, λ, and refractive index, m (Hansen and Travis 1974).

Using effective radius r_e defined by Hansen and Travis (1974),

$$r_e = \frac{\int_0^\infty \pi r^3 n(r) dr}{\int_0^\infty \pi r^2 n(r) dr} \quad \text{(A.4)}$$

and the definition of liquid water content, w,

$$w = \frac{4}{3} \pi \rho_w \int_0^\infty r^3 n(r) dr, \quad \text{(A.5)}$$

we have

$$\tau(\lambda) = \frac{3\tilde{Q}_{\text{ext}}}{4\rho_w} \int_0^h \frac{w}{r_e} dh, \quad \text{(A.6)}$$

where $\tilde{Q}_{\text{ext}}$ is the average of Q_{ext} over the droplet size distribution. Defining liquid water path (LWP) as

$$LWP = \int_0^h w dh' \quad \text{(A.7)}$$

then cloud optical thickness is linked to cloud effective radius by

$$\tau(\lambda) = 0.75 \tilde{Q}_{\text{ext}} \frac{\text{LWP}}{\rho_w r_e}. \quad \text{(A.8)}$$

b. Droplet size distribution

The standard gamma distribution (Hansen 1971) is used in this paper for cloud droplet size distributions,

$$n(r) = C r^{(1-3b)/b} e^{-r/(ab)}, \quad \text{(A.9)}$$

where C is a constant, $n(r)dr$ is the number of particles per unit volume with radius between r and $r + dr$. It has the simple properties that the two parameters a and b represent the mean effective radius (average weighted by cross section) and the effective variance for this size distribution; that is, $r_e = a$ and $v_e = b$ (Hansen and Travis 1974). It also links effective radius, r_e, and the mean radius, r_m, in a simple relationship

$$r_e = r_m/(1 - 2b), \quad \text{(A.10)}$$

where $r_m = \int_0^\infty r n(r) dr / \int_0^\infty n(r) dr$ and is often the value reported by in situ measurements.

TABLE A.1. $\tilde{\omega}_0$, g, K, and $(\tau' - \tau_0)/\tau_0$ for different cloud droplet size.

Radius (μm)	$\tilde{\omega}_0$	g	K	$(\tau' - \tau_0)/\tau_0$
1.0	0.99999975	0.783137	0.641	−0.359
2.0	0.99999941	0.792963	0.672	−0.328
5.0	0.99999856	0.843773	0.890	−0.110
10.0	0.99999722	0.860949	1.000	0.0
15.0	0.99999592	0.867576	1.050	0.050
20.0	0.99999465	0.871198	1.080	0.080
30.0	0.99999221	0.874955	1.112	0.112
35.0	0.99999089	0.875930	1.121	0.121

This size distribution can relate r_e with cloud liquid water content w explicitly. The definition (A.5) can be rewritten as

$$w = kr_e^3\rho_w N, \qquad \text{(A.11)}$$

where $k = 4\pi(1 - b)(1 - 2b)/3$ and $N = \int_0^\infty n(r)dr$.

According to observation, for most clouds, b ranges from 0.10 to 0.20 (Hansen 1971). For example, $b = 0.111$ for fair weather cumulus and 0.193 for stratus.

c. *Droplet radius effect on ISCCP τ retrieval*

To estimate the droplet radius effect on τ, we rewrite Eq. (2) as $\tau' = K\tau$, where $K = (1 - \tilde{\omega}_0 g)/(1 - \tilde{\omega}_0' g')$. Then the relative error caused by 10-μm water droplet assumption used in ISCCP can be easily estimated. The relative error is $(\tau' - \tau_0)/\tau_0 = (g' - g_0)/(1 - g')$, where τ_0 is the optical thickness of ISCCP analysis, g_0 is the asymmetry factor for 10-μm water droplet. Table A.1 lists the values of $\tilde{\omega}_0$, g, K, and $(\tau' - \tau_0)/\tau_0$ for different cloud droplet radii.

REFERENCES

Ackerman, S. A., and W. L. Smith, 1990: Inferring cloud microphysical properties from high resolution spectral measurements in the 8-13 mu window region. Preprints, *7th Conf. Atmos. Radiation,* San Francisco, Amer. Meteor. Soc., 6-8.

Albrecht, B. A., 1989: Aerosols, cloud microphysics and fractional cloudiness. *Science,* **245,** 1227-1230.

Arking, A., and J. D. Childs, 1985: Retrieval of cloud cover parameters from multispectral satellite images. *J. Climate Appl. Meteor.,* **24,** 322-333.

Betts, A. K., and Harshvardhan, 1987: Thermodynamic constraint on the cloud liquid water feedback in climate models. *J. Geophys. Res.,* **92,** 8483-8485.

Blau, H. H., R. P. Espinola, and E. C. Reifenstein, 1966: Near infrared scattering by sunlit terrestrial clouds. *Appl. Opt.,* **5,** 555-564.

Brest, C. L., and W. B. Rossow, 1992: Radiometric calibration and monitoring of NOAA AVHRR data for ISCCP. *Int. J. Remote Sens.,* **13,** 235-273.

Browell, E. V., G. L. Gregory, R. C. Harriss, and V. W. J. H. Kirchhoff, 1990: Ozone and aerosol distributions over the Amazon Basin during the wet season. *J. Geophys. Res.,* **95,** 16 887-16 902.

Brown, J. W., O. B. Brown, and R. H. Evans, 1992: Calibration of AVHRR infrared channels: A new approach to nonlinear correction. *J. Geophys. Res.,* submitted.

Brown, O. B., J. W. Brown, and R. H. Evans, 1985: Calibration of Advanced Very High Resolution Radiometer infrared observations. *J. Geophys. Res.,* **90,** 11 667-11 677.

Cess, R. D., G. L. Potter, J. P. Blanchet, G. J. Boer, A. D. Del Genio, M. Deque, V. Dymnikov, V. Galin, W. L. Gates, S. J. Ghan, J. T. Kiehl, A. A. Lacis, H. Le. Treut, Z. X. Li, X. Z. Liang, B. J. McAvaney, V. P. Meleshko, and J. F. B. Mitchell, 1990: Interpretation of climate feedback processes in 19 atmospheric general circulation models. *J. Geophys. Res.,* **95,** 16 601-16 615.

Chang, F-L., and J. A. Coakley, 1993: Estimating errors in fractional cloud cover obtained with infrared threshold methods. *J. Geophys. Res.,* **98,** 8825-8839.

Charlson, R. J., S. E. Schwartz, J. M. Hales, R. D. Cess, J. A. Coakley, Jr., J. E. Hansen, and D. J. Hofmann, 1992: Climate forcing by anthropogenic aerosols. *Science,* **255,** 423-430.

Coakley, J. A., 1991: Reflectivities of uniform and broken layered cloud. *Tellus,* **43**(B), 420-443.

——, and F. P. Bretherton, 1982: Cloud cover from high-resolution scanner data: Detecting and allowing for partially filled fields of view. *J. Geophys. Res.,* **87,** 4917-4932.

——, and D. G. Baldwin, 1984: Towards the objective analysis of clouds from satellite imagery data. *J. Climate Appl. Meteor.,* **23,** 1065-1099.

——, and R. Davies, 1986: The effect of cloud sides on reflected solar radiation as deduced from satellite observations. *J. Atmos. Sci.,* **43,** 1025-1035.

——, and T. Kobayashi, 1989: Broken cloud biases in albedo and surface insolation derived from satellite imagery data. *J. Climate,* **2,** 721-730.

Curry, J. A., and G. F. Herman, 1985: Infrared radiative properties of summertime arctic stratus clouds. *J. Appl. Meteor.,* **24,** 525-538.

——, C. D. Ardeel, and L. Tian, 1990: Liquid water content and precipitation characteristics of stratiform clouds as inferred from satellite microwave measurements. *J. Geophys. Res.,* **95,** 16 659-16 671.

Davies, R., 1978: The effect of finite geometry on the three-dimensional transfer of solar irradiance in clouds. *J. Atmos. Sci.,* **35,** 1712-1725.

——, 1984: Reflected solar radiances from broken cloud scenes and the interpretation of scanner measurements. *J. Geophys. Res.,* **89,** 1259-1266.

Dinger, J. E., H. B. Howell, and T. A. Wojciechowski, 1970: On the source and composition of cloud condensation nuclei in the subsident air mass over the North Atlantic. *J. Atmos. Sci.,* **27,** 791-797.

Durbin, W. G., 1959: Droplet sampling in cumulus clouds. *Tellus,* **11,** 202-215.

Goody, R. M., and J. Walker, 1972: *Atmospheres.* Prentice-Hall, 150 pp.

——, and Y. L. Yung, 1989: *Atmospheric Radiation, Theoretical Basis.* 2d ed. Oxford University Press, 519 pp.

Han, Q., 1992: Global survey of effective particle size in liquid water cloud by satellite observations. Ph.D. dissertation, Columbia University, 205 pp.

Hansen, J. E., 1971: Multiple scattering of polarized light in planetary atmospheres. Part II: Sunlight reflected by terrestrial water clouds. *J. Atmos. Sci.,* **28,** 1400-1426.

——, and J. B. Pollack, 1970: Near-infrared light scattering by terrestrial clouds. *J. Atmos. Sci.,* **27,** 265-281.

——, and L. D. Travis, 1974: Light scattering in planetary atmospheres. *Space Sci. Rev.,* **16,** 527-610.

——, and A. A. Lacis, 1990: Sun and dust versus greenhouse gases: An assessment of their relative roles in global climate change. *Nature,* **346,** 713-719.

Harshvardhan, 1982: The effect of brokenness on cloud-climate sensitivity. *J. Atmos. Sci.,* **39,** 1853-1861.

Hoppel, W. A., J. E. Dinger, and R. E. Ruskin, 1973: Vertical profiles of CCN at various geographical locations. *J. Atmos. Sci.,* **30,** 1410-1420.

Hovis, W. A., and M. Tobin, 1967: Spectral measurements from 1.6 μ to 5.4 μ of natural surfaces and clouds. *Appl. Opt.*, **6**, 1399–1402.

Jensen, J. B., A. M. Blyth, M. B. Baker, and P. H. Austin, 1985: Small-scale variability in warm continental cumulus clouds. *J. Atmos. Sci.*, **42**, 1123–1138.

King, M. D., and Harshvardhan, 1986: Comparative accuracy of selected multiple scattering approximation. *J. Atmos. Sci.*, **43**, 784–801.

Kobayashi, T., 1993: Effects due to cloud geometry on biases in the albedo derived from radiance measurements. *J. Climate*, **6**, 120–128.

Lacis, A. A., and J. E. Hansen, 1974: A parameterization for the absorption of solar radiation in the earth's atmosphere. *J. Atmos. Sci.*, **31**, 118–133.

——, and V. Oinas, 1991: A description of the correlated *k*-distribution method for modeling non-grey gaseous absorption, thermal emission, and multiple scattering in vertically inhomogeneous atmospheres. *J. Geophys. Res.*, **96**, 9027–9063.

Leaitch, W. R., J. W. Strapp, H. A. Wiebe, and G. A. Isaac, 1983: Measurements of scavenging and transformation of aerosol inside cumulus. *Precipitation Scavenging, Dry Deposition, and Resuspension*, H. R. Pruppacher, R. G. Semonin and W. G. N. Slinn, Eds., Elsevier, 53–66.

Liou, K. N., 1980: *An Introduction to Atmospheric Radiation. International Geophysics Series.* Vol. 25, Academic Press, 392 pp.

MacCracken, M. C., R. D. Cess, and G. L. Potter, 1986: Climatic effects of anthropogenic Arctic aerosols: An illustration of climate feedback mechanisms with one- and two-dimensional climate models. *J. Geophys. Res.*, **91**, 14 445–14 450.

Mason, B. J., 1971: *The Physics of Clouds* (2nd edition). Clarendon, 671 pp.

McClatchey, R. A., R. W. Fenn, J. E. A. Selby, F. E. Volz, and J. S. Garing, 1972: Optical Properties of the Atmosphere. Air Force Cambridge Research Laboratories, AFCRL-72-0497, Environmental Research Paper, No. 411, 108 pp.

Minnis, P., and E. F. Harrison, 1984: Diurnal variability of regional cloud and clear-sky radiative parameters derived from GOES data. Part I: Analysis method. *J. Climate Appl. Meteor.*, **23**, 993–1011.

——, P., P. W. Heck, D. F. Young, C. W. Fairall, and J. B. Snider, 1992: Stratocumulus cloud properties derived from simultaneous satellite and island-based instrumentation during FIRE. *J. Appl. Meteor.*, **31**, 317–339.

——, ——, and ——, 1993: Inference of cirrus cloud properties from satellite-observed visible and infrared radiances. Part II: Verification of theoretical cirrus radiative properties. *J. Atmos. Sci.*, **50**, 1305–1322.

Nakajima, T., and M. D. King, 1990: Determination of the optical thickness and effective particle radius of clouds from reflected solar radiation measurements. Part I: Theory. *J. Atmos. Sci.*, **47**, 1878–1893.

——, ——, and J. D. Spinhirne, 1991: Determination of the optical thickness and effective particle radius of clouds from reflected solar radiation measurements. Part II: Marine stratocumulus observations. *J. Atmos. Sci.*, **48**, 728–750.

Neckel, H., and D. Labs, 1984: The solar radiation between 3300 and 12500 Å. *Solar Phys.*, **90**, 205–258.

Nicholls, S., 1984: The dynamics of stratocumulus: Aircraft observations and comparisons with a mixed layer and model. *Quart. J. Roy. Meteor. Soc.*, **110**, 783–820.

Noonkester, V. R., 1984: Droplet spectra observed in marine stratus cloud layers. *J. Atmos. Sci.*, **41**, 829–845.

Platt, C. M. R., 1989: The role of cloud microphysics in high-cloud feedback effects on climate change. *Nature*, **341**, 428–429.

Pollack, J. B., D. W. Strecker, F. C. Witteborn, E. F. Erickson, and B. J. Baldwin, 1978: Properties of the clouds of venus, as inferred from airborne observations of its near-infrared reflectivity spectrum. *Icarus*, **34**, 28–45.

Prabhakara, C., R. S. Fraser, G. Dalu, M. L. C. Wu, and R. J. Curran, 1988: Thin cirrus clouds: Seasonal distribution over oceans deduced from *Nimbus-4* IRIS. *J. Appl. Meteor.*, **27**, 379–399.

Prospero, J. M., R. J. Charlson, V. Mohnen, R. Jaenicke, A. C. Delany, J. Moyers, W. Zoller, and K. Rahn, 1983: The atmospheric aerosol system: An overview. *Rev. Geophys. Space Phys.*, **21**, 1607–1629.

Pruppacher, H. R., and J. D. Klett, 1978: *Microphysics of Clouds and Precipitation.* Reidel, Dordrecht, 714 pp.

Radke, L. F., and J. A. Coakley, Jr., and M. D. King, 1989: Direct and remote sensing observations of the effects of ships on clouds. *Science*, **246**, 1146–1149.

Rawlins, F., and J. S. Foot, 1990: Remotely sensed measurements of stratocumulus properties during FIRE using the C130 aircraft multi-channel radiometer. *J. Atmos. Sci.*, **47**, 2488–2503.

Rogers, R. R., and M. K. Yau, 1989: *A Short Course in Cloud Physics.* 3rd edition, Pergamon Press, 293 pp.

Rossow, W. B., 1978: Cloud microphysics: Analysis of the clouds of Earth, Venus, Mars and Jupiter. *Icarus*, **36**, 1–50.

——, 1989: Measuring cloud properties from space: A review. *J. Climate*, **2**, 201–213.

——, and A. A. Lacis, 1990: Global, seasonal cloud variations from satellite radiance measurements. Part II: Cloud properties and radiative effects. *J. Climate*, **3**, 1204–1253.

——, and R. A. Schiffer, 1991: ISCCP cloud data products. *Bull. Amer. Meteor. Soc.*, **72**, 2–20.

——, and L. C. Garder, 1993a: Cloud detection using satellite measurements of infrared and visible radiances for ISCCP. *J. Climate*, **6**, 2341–2369.

——, and ——, 1993b: Validation of ISCCP cloud detections. *J. Climate*, **6**, 2370–2393.

——, E. Kinsella, A. Wolf, and L. Garder, 1987: International satellite cloud climatology project (ISCCP) description of reduced resolution radiance data. WMO/TD-No. 58, 143 pp.

——, L. C. Garder, and A. A. Lacis, 1989: Global, seasonal cloud variations from satellite radiance measurements. Part I: Sensitivity of analysis. *J. Climate*, **2**, 419–458.

——, ——, P. J. Lu, and A. W. Walker, 1991: International Satellite Cloud Climatology Project (ISCCP) Documentation of Cloud Data. WMO/TD-No. 266 (Revised). World Meteorological Organization, Geneva, 76 pp. + three appendices.

——, A. W. Walker, and L. C. Garder, 1993: Comparison of ISCCP and other cloud amounts. *J. Climate*, **6**, 2394–2418.

Ryan, B. T., H. H. Blau, P. C. Thuna, M. L. Cohen, and G. D. Roberts, 1972: Cloud microstructure as determined by optical cloud particle spectrometer. *J. Appl. Meteor.*, **11**, 149–156.

Schiffer, R. A., and W. B. Rossow, 1985: ISCCP global radiance data set: A new resource for climate research. *Bull. Amer. Meteor. Soc.*, **66**, 1498–1505.

Schwartz, S. E., 1988: Are global cloud albedo and climate controlled by marine phytoplankton? *Nature*, **336**, 441–445.

Seze, G., and W. B. Rossow, 1991: Time-cumulated visible and infrared radiance histograms used as descriptors of surface and cloud variations. *Int. J. Remote Sens.*, **12**, 877–920.

Singleton, F., and D. J. Smith, 1960: Some observations of drop-size distributions in low layer clouds. *Quart J. Roy. Meteor. Soc.*, **86**, 454–467.

Slingo, A., 1988: Can plankton control climate? *Nature*, **336**, 421.

Somerville, R. C., and L. A. Remer, 1984: Cloud optical thickness feedbacks in the CO2 climate problem. *J. Geophys. Res.*, **89**, 9668–9672.

Squires, P., 1958: The microstructure and colloidal stability of warm clouds. Part II—The cause of the variations in microstructure. *Tellus*, **10**, 262–271.

Stephens, G. L., 1978: Radiation profiles in extended water clouds. I: Theory. *J. Atmos. Sci.*, **35**, 2111–2122.

Stull, R. B., 1988: *An Introduction to Boundary Layer Meteorology.* Kluwer Academic, 666 pp.

Takano, Y., and K. N. Liou, 1989: Solar radiative transfer in cirrus clouds. Part II: Theory and computation of multiple scattering in an anisotropic medium. *J. Atmos. Sci.*, **46**, 20–36.

Taylor, J. P., 1992: Sensitivity of remotely sensed effective radius of cloud droplets to changes in LOWTRAN version. *J. Atmos. Sci.*, **49**, 2564–2569.

Telford, J. W., and P. B. Wagner, 1981: Observations of condensation growth determined by entity type mixing. *Pure Appl. Geophys.*, **119**, 934–965.

Thekaekara, M. P., 1974: Extraterrestrial solar spectrum, 3000–6100 Å at 1-Å intervals. *Appl. Opt.*, **13**, 518–522.

Tselioudis, G., 1992: Global patterns of cloud optical thickness variation with temperature and the implications for climate change. PhD thesis, Columbia University, 193 pp.

——, W. B. Rossow, and D. Rind, 1992: Global patterns of cloud optical thickness variation with temperature. *J. Climate*, **5**, 1484–1495.

Twomey, S., 1977: Atmospheric aerosols. *Developments in Atmospheric Science, Vol. 7, Elsevier, 302 pp.*

——, *and T. A. Wojciechowski, 1969: Observations of the geographical variation of cloud nuclei. J. Atmos. Sci.*, **26**, 684–688.

——, and T. Cocks, 1982: Spectral reflectance of clouds in the near-infrared: Comparison of measurements and calculations. *J. Meteor. Soc. Japan*, **60**, 583–592.

——, and ——, 1989: Remote sensing of cloud parameters from spectral reflectance in the near-infrared. *Beitr. Phys. Atmos.*, **62**, 172–179.

——, M. Piepgrass, and T. L. Wolfe, 1984: An assessment of the impact of pollution on global cloud albedo. *Tellus*, **36B**, 356–366.

van de Hulst, H. C., 1980: *Multiple Light Scattering, Tables, Formulas, and Applications.* Vol. 1. Academic Press, 739 pp.

Wallace, J. M., and P. V. Hobbs, 1977: *Atmospheric Science—An Introductory Survey.* Academic Press, 467 pp.

Warren, S. G., C. J. Hahn, J. London, R. M. Chervine, and R. L. Jenne, 1986: Global distribution of total cloud cover and cloud type amounts over land. NCAR Technical Note, NCAR/TN-273+STR/DOE Tech. Rep. ER/60085-H1, 29 pp. + 200 maps. [NTIS number DE87-00-6903.]

——, ——, ——, ——, and ——, 1988: Global distribution of total cloud cover and cloud type amounts over ocean. NCAR Technical Note, NCAR/TN-317+STR/DOE Tech. Rep. ER-0406, 42 pp + 170 maps. [NTIS number DE90-00-3187.]

Weickmann, H. K., and H. J. aufm Kampe, 1953: Physical properties of cumulus clouds. *J. Meteor.*, **10**, 204–211.

Welch, R. M., and B. A. Wielicki, 1984: Stratocumulus cloud field reflected fluxes: The effect of cloud shape. *J. Atmos. Sci.*, **41**, 3085–3103.

——, and ——, 1989: Reflected fluxes from broken clouds over a Lambertian surface. *J. Atmos. Sci.*, **46**, 1384–1395.

Wielicki, B. A., and L. Parker, 1992: On the determination of cloud cover from satellite sensors: The effect of sensor spatial resolution. *J. Geophys. Res.*, **97**, 12 799–12 823.

——, J. T. Suttles, A. J. Heymsfield, R. M. Welch, J. D. Spinhirne, M. C. Wu, D. O. Starr, L. Parker, and R. F. Arduini, 1990: The 27–28 October 1986 FIRE IFO cirrus case study: Comparison of radiative transfer theory with observations by satellite and aircraft. *Mon. Wea. Rev.*, **118**, 2356–2376.

Wigley, T. M. L., 1991: Could reducing fossil-fuel emissions cause global warming? *Nature*, **349**, 503–506.

Wylie, D. P., and W. P. Menzel, 1991: A cirrus cloud climatology from NOAA/HIRS. *Palaeogeogr., Palaeoclimatol., Palaeoecol.*, **90**, 49–53.